**TECHNISCHE
UNIVERSITÄT
WIEN**
Vienna University of Technology

Diplomarbeit

A New Method for Monitoring Clean-in-Place Processes by Using Quantum Cascade Lasers

Ausgeführt am Institut für

Chemische Technologien und Analytik

der Technischen Universität Wien

unter der Anleitung von

Ao. Univ. Prof. DI Dr. Bernhard Lendl

und

DI Dr. Markus Brandstetter

durch

Andreas Genner, BSc

Hauptstraße 129, A-2831 Scheiblingkirchen

_____   _____
Datum   Unterschrift

Zusammenfassung

In dieser Arbeit wird ein neues Messprinzip zur Beobachtung von Reinigungsprozessen von Rührkesseln in der pharmazeutischen Industrie vorgestellt. Während bisher erst am Ende des Reinigungsprozesses der gesamte organische Kohlenstoffgehalt der Reinigungsflüssigkeit bestimmt wird, kann ein Äquivalenzwert durch den Einsatz der Infrarotspektroskopie nahezu kontinuierlich gemessen werden und folglich der gesamte Reinigungsprozess optimiert werden. Bei diesem Sensor wird ein Quantenkaskaden Laser mit externer Kavität im Bereich zwischen 1030–1230 cm^{-1} als Lichtquelle eingesetzt. Das Prozesswasser wird über ein Fließ-Injektionssystem in eine CaF$_2$ Flusszelle mit 165 µm Schichtdicke injeziert und das transmittierte Licht mit einem MCT-Detektor gemessen. Die Performance und Anwendbarkeit dieses Sensors wird anhand eines Laborreaktors, einer industrie-nahen Anlage an der Technischen Universität Wien sowie bei einem Kooperationspartner (CMC Biologics, Kopenhagen) gezeigt. Um ressourcenschonend zu Arbeiten werden anstatt zeitaufwändiger Fermentationen zwei typische Kohlenstoffquellen, nämlich Glycerol und Xanthan, als Kontaminationen eingesetzt. Weiters wird die Herstellung von oberflächen-emittierenden Quantenkaskadenlasern mit ringförmiger Kavität im Bereich 1470–1530 cm^{-1} gezeigt, um in Zukunft auch die Absorption von Proteinen im Prozesswasser bestimmen zu können.

Abstract

This thesis introduces a new measurement principle to monitor cleaning processes of stirrer vessels in the pharmaceutical industry. Until now, the cleanliness of a vessel is evaluated by quantifying the total organic carbon of the cleaning liquid at the end of the cleaning sequence. With infrared spectroscopy, in contrast, it is possible to monitor the cleaning liquid continuously, allowing to shorten the cleaning process. The sensor is based on an external quantum cascade laser emitting radiation in the range of 1030–$1230\,cm^{-1}$. Samples from the process stream are continuously injected into a $165\,\mu m$ flow cell whereas the windows are made out of CaF_2. Finally, the transmitted radiation is quantified by an MCT-detector. The performance and applicability of the sensor are evaluated at a laboratory vessel, an industrial-scale plant at the Vienna University of Technology as well as at a co-operation partner (CMC Biologics, Copenhagen). In order to save resources and time consuming fermentations, two typical carbon sources, namely glycerol and xanthan gum, are used as contamination substances. Moreover, the manufacturing process of ring cavity surface emitting lasers in the wavelength range of 1470–$1530\,cm^{-1}$ is shown. Its intention is to quantify proteins in the process stream in the future as well.

Acknowledgements

Special thanks go to

··· M. Harasek, B. Lendl and G. Strasser for supporting and enabling this interdisciplinary thesis, combining state-of-the-art technology with an industrial application

··· M. Brandstetter and C. Schwarzer for their excellent supervision and their technical support, especially when things didn't work in the lab as they should have.

Moreover, I would like to thank

··· the colleagues in the working group of B. Lendl:

C. Gasser, C. Koch, C. Kristament, H. Moser, G. Ramer, C. Reidl-Leuthner, W. Ritter, J. Ofner, W. Tomischko, C. Wagner, J. P. Wazlawek and M. El-Zahry,

"... in a few years, all great physical constants will have been approximately estimated, and that the only occupation which will be left to men of science will be to carry these measurements to another place of decimals."

James C. Maxwell

Introductory Lecture on Experimental Physics held at Cambridge in October 1871, http://en.wikiquote.org/wiki/James_Clerk_Maxwell

Contents

Glossary

$A_{(\lambda)}$ . . . . Absorption $A_{(\lambda)} = -\log \frac{I_{(\lambda)}}{I_{0,(\lambda)}} = \epsilon_{(\lambda)}\, c\, l$ [AU]

$\alpha_{externalgrating}$ . . . External grating losses $[\mathrm{cm}^{-1}]$

$\alpha_{grating}$ . . . . Grating losses $[\mathrm{cm}^{-1}]$

α_{mirror} . . . . Mirror losses $[\mathrm{cm}^{-1}]$

$\alpha_{substrate}$ . . . . . . Substrate losses $[\mathrm{cm}^{-1}]$

$\alpha_{surface}$ . . . . Surface losses $[\mathrm{cm}^{-1}]$

α_{total} . . . . Total losses $[\mathrm{cm}^{-1}]$

$\alpha_{waveguide}$ . . . . . . Waveguide losses $[\mathrm{cm}^{-1}]$

Γ . . . . Confinement factor $\Gamma = \frac{\int_{act} |E|^2 dz}{\int_{-\infty}^{\infty} |E|^2 dz}$

c . . . . Vacuum speed of light ($299\,792\,458\,\mathrm{m\,s}^{-1}$)

$\epsilon_{(\lambda)}$ . . . . Wavelength dependent molar absorption coefficient $[\mathrm{L\,mol}^{-1}\,\mathrm{cm}^{-1}]$

h . . . . .Planck constant $(6.626\,069\,57 \times 10^{-34}\,\mathrm{J\,s})$

$I_{0,(\lambda)}$ . . . . .Background single beam intensity [a.u.]

$I_{(\lambda)}$ . . . . .Sample single beam intensity [a.u.]

J_{th} . . . . .Threshold current density $[\mathrm{A\,cm}^{-2}]$

k_B . . . . .Boltzmann constant, $(13\,806\,488 \times 10^{-23}\,\mathrm{J\,K}^{-1})$

L_σ . . . . .Spectral radiance $[\mathrm{Wm}^{-2}\mathrm{sr}^{-1}(\mathrm{cm}^{-1})^{-1}]$

λ . . . . .Wavelength $[\mathrm{\mu m}]$

l . . . . .Optical path length $[\mathrm{\mu m}]$

μ . . . . .Reduced mass $\mu = \frac{m_A m_B}{m_A + m_B}$ $[\mathrm{kg}]$

$\tilde{\nu}$ . . . . .Wavenumber $[\mathrm{cm}^{-1}]$

Acronyms

AAS . . . . .Atomic absorption spectroscopy

ADC . . . . .Analog digital converter

ATLAS . . . . . . .Advanced Total Lab Automation Software

CIP . . . . .Clean-in-Place

DBR . . . . .Distributed Bragg reflector

DC . . . . .Direct current

DFB . . . . .Distributed feedback

DLC . . . . .Diamond-like carbon

EC-QCL . . . . . .External cavity - quantum cascade laser

FIA . . . . .Flow injection analysis

FIR . . . . .Far infrared

FP . . . . .Fabry-Perot

FTIR . . . . .Fourier transform infrared

GC . . . . .Gas chromatography

HPLC . . . . .High pressure liquid chromatography

IR . . . . .Infrared

LIV . . . . .Light intensity (L) - current (I) - voltage (V)

LOD . . . . .Limit of detection

MBE . . . . .Molecular beam epitaxy

MCT . . . . .Mercury cadmium telluride

MIR . . . . .Mid infrared

MOCVD . . . . . .Metalorganic chemical vapor deposition

MOVPE . . . . . .Metalorganic vapor phase epitaxy

MS . . . . .Mass spectroscopy

NDIR . . . . .Nondispersive infrared sensor

NIR . . . . .Near infrared

PATOV . . . . . . .Process Analytical Technology Unit for Online Verification of
the CIP Process in the Pharmaceutical Industry

PCB . . . . .Printed circuit board

PE . . . . .Polyethylene

PLC . . . . .Programmable logic controller

PMMA . . . . . . .Poly(methyl methacrylate)

PTFE . . . . .Polytetrafluorethylene

QCD . . . . .Quantum cascade detector

QCL . . . . .Quantum cascade laser

RIE . . . . .Reactive ion etching

ring-CSEL . . . . .Ring-cavity surface emitting laser

TEC . . . . .Thermoelectric cooling

TIC . . . . .Total inorganic carbon

TOC . . . . .Total organic carbon

WFI . . . . .Water for injection

Chapter 1.

Introduction and Theory

1.1. Motivation and Scope

Product quality and purity are the the most important parameters in the biopharmaceutical industry. For the manufacturer it is of utmost importance to fit the customer's requirements as well as keeping the production costs at a minimum. While industries with high throughput, such as the cement or the petroleum industry, reduce their costs with continuous flow reactors operated 24/7, the biopharmaceutical industry uses typically batch reactors. The advantages of that reactor type are the lower costs of infrastructure, the applicability to different products and the smaller minimum purchase volume. On the other hand, sequential production causes increased down time of the production process as the vessels have to be cleaned after each batch and setup for the next. With a proper performed cleaning process, cross

contamination of the products can be elimited. However, cleaning of equipment is time consuming, requires cleaning agents and manpower.

A biopharmaceutical process can be optimized at several stages of the production. For example, the bacteria or fungi can be modified to feature a higher yield, less side products or faster growth. Another approach is to simplify and speed up the purification step of the product. Moreover, production costs can be reduced if the down times of a reactor are minimized. Within this thesis, it was intended to develop a measuring technology for shortening the cleaning time of the process equipment, thereby increasing the productivity of the whole system.

1.2. Clean-in-Place

Clean-in-Place (CIP) implies all the technologies that are required to enable an automated cleaning of the process equipment without disassembling the system into its components. It typically includes water for injection (WFI)-tanks, cleaning agents (caustic, acid, defoamers, surfactants, ...), pipes, pumps and valves for transporting the cleaning agents, equipment for distributing the liquid on the surface of the vessel to be cleaned (spray ball) and automation equipment (programmable logic controller (PLC)). CIP was first applied for cleaning the pipelines of a milking system back in the 1950s and was soon adopted in the food and beverage industry. In the pharmaceutical industry the CIP technology came up in the late 1980s and became more and more important in the following years [1].

A very simple configuration of a CIP facility is shown in fig. 1.1. It consists of the already mentioned WFI tank, the cleaning agents, the tank to be cleaned, pipes, valves and pumps.
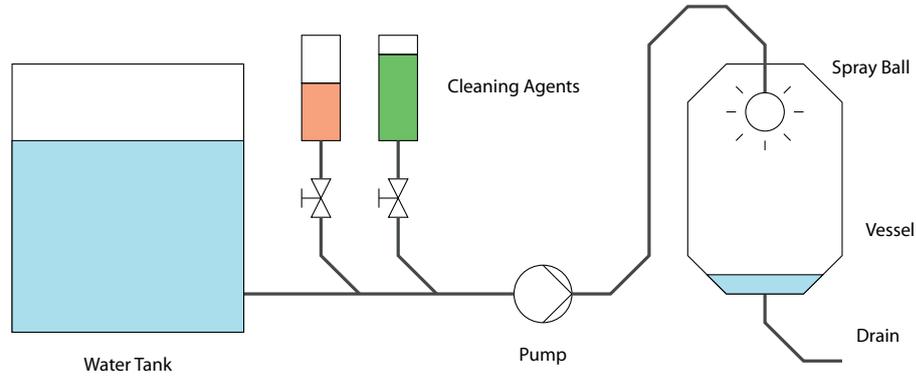
Figure 1.1.: Basic CIP setup consisting of a WFI tank, cleaning agents, a pump, a spray ball and the vessel to be cleaned.

With these few parts, it is already possible to run a CIP process. A standard version of the CIP process includes the following steps: At first, the vessel to be cleaned is flushed with water whereas the cleaning is dominated by the mechanical interaction. During the next step, caustic is pumped into the vessel to decompose remaining residuals such as proteins, oils or fats. The caustic step is then followed by an acidic one to oxidize and passivate the surface of the vessel. Finally, WFI is flushed through the system to wash the remaining acid out of the system and to achieve a neutral pH again.

Before the next batch can be processed in the cleaned vessel, it has to be verified that all residuals are indeed removed. This is a crucial step, as it determines the actual contamination state. To do so, different techniques are available to analyze

the waste water whereas specific and non-specific methods are available:

Specific Methods: This includes for example high pressure liquid chromatography (HPLC), gas chromatography (GC), atomic absorption spectroscopy (AAS), mass spectroscopy (MS) [2] or reflectance infrared spectroscopy [3–6]. Their advantage is that they deliver quantitative information for individual contaminants. On the other hand, they require advanced sample preparation, are typically performed offline and can be time consuming.

Non-Specific Methods: Measuring the pH, the conductivity, counting the particles [2] or recording an UV/Vis-spectrum [7] are, compared to specific methods, much faster and can be implemented as inline sensors very easily. However, they don't deliver contaminant specific information and can be dominated by the cleaning agents.

Another widely used method is to determine the total organic carbon (TOC). Although this non-specific method is slightly slower than others, it delivers the carbon content of the cleaning fluid and therefore a more precise value for the cleanliness of a vessel.

1.2.1. TOC Analysis - State of the Art

The basic principle of quantifying the TOC content is to oxidize all the carbon in a sample and then detect the produced CO_2 [8, 9]. It has to be mentioned that

carbon can also occur as inorganic species, mainly as carbonate. To get a correct TOC value, the carbonate has to be removed in the first step. This is done by adding acid (e.g. HCl, H_2SO_4 or H_3PO_4) to the sample and purging with a suiting inert gas like He, N_2 or Ar. The produced CO_2 is then measured with a nondispersive infrared sensor (NDIR) and it represents the total inorganic carbon (TIC). For the following oxidation of the carbon, two different techniques are available:

Combustion: The purged sample is injected into a combustion reactor and oxidized at temperatures higher than $1000\,°C$. The high reaction temperatures can be reduced by filling the reaction chamber with catalysts like CoO, Cr_2O_3, V_2O_5, WO_3 or others whereas the required temperature can be lowered down to $800\,°C$. The generated CO_2 is finally quantified with an NDIR sensor [8].

Chemical oxidation: The sample is oxidized by adding either $K_2S_2O_8$ or a mixture of $K_2Cr_2O_7$ and H_2SO_4. Different established methods are available whereas heating to temperatures between $100\,°C$ and $170\,°C$ is typically required. When persulfate is used as oxidizer, UV light can also be applied as activator. The TOC value can be measured by quantifying the produced CO_2 or by titration of the remaining oxidizer [8].

Quantifying the TOC content of a sample is nowadays a routine analysis and devices are available from many different companies (e.g. Mettler-Toledo International Inc., GE Analytical Instruments Inc., Shimadzu Corp., Hach-Lange GmbH, Horiba Jobin Yvon GmbH). They allow a limit of detection (LOD) down to the ppb-region, automated sample preconditioning, such as auto-dilution and acidification, and even

on-line measurements are possible. On the other hand, the measurement principle doesn't allow high throughput rates as the acidification and oxidation are the time limiting operations. The typical measurement time is in the range of 3–4 min and depends mainly on the employed oxidation method.

An example of implementing a TOC analyzer into a CIP system is shown in [10]. The aim of the project was to show the combination of TOC analysis and conductivity measurements in a CIP unit. The first wash cycles were only monitored by measuring the conductivity as the carbon content would have exceeded the maximum limit of the TOC analyzer. While the wash cycles used caustic and acid as detergents, the final rinse was performed with pure water. When the conductivity reached a certain limit, the sample for measuring the TOC concentration was drawn and analyzed.

1.2.2. PATOV-Project

The intention of the project 'Process Analytical Technology Unit for Online Verification of the CIP Process in the Pharmaceutical Industry' (PATOV) (`http://www.patov.eu/`) is optimizing the control of the CIP process by monitoring the cleanliness of the cleaning liquid. The initial approach was quantifying the TOC concentration, as it is an established and accepted method in the pharmaceutical industry. The first experiments showed that implementing a TOC analyzer is not the favored method as it is time consuming and supports only a limited concentration range. Other non-specific methods could be applied, but many substances are still impossible to detect with these techniques. Glycerol, for example, is a widely used carbon-source for fermentation that dissolves in water (no particles), doesn't influence the pH, doesn't

change the conductivity and is colorless. It could be detected with specific methods, but on the other hand, these techniques are even more time consuming than measuring the TOC value.

Contaminants, which occur in biopharmaceutical production are typically carbon based molecules. Thus, a measurement technique that is sensitive to carbon specific properties has to be applied. Another requirement is the much lower measurement time than available TOC analyzers supply. A suitable method for solving this problem is infrared spectroscopy because it is an optical technique, allowing a high temporal resolution and molecule specific information. Therefore, the new goal of PATOV was the development of an innovative measurement technique that returns a value, which correlates to the carbon content of the cleaning liquid.

1.3. Infrared Spectroscopy

Infrared (IR) spectroscopy is an optical spectroscopy method which uses the electromagnetic spectrum within the wavelength region 0.78–1000 µm. On the high-frequency side, it is located next to the visible spectrum and at the low-frequency side it is followed by the microwave-region. The IR-region itself can be differentiated into three parts, namely the near infrared (NIR), mid infrared (MIR) and the far infrard (FIR). The corresponding spectral ranges are, according to [11], 0.78–3 µm for the NIR, 3–50 µm for the MIR and 50–1000 µm for the FIR. Moreover, the FIR corresponds mainly to the rotations of molecules, the MIR covers the fundamental vibrations and the NIR is assigned to its overtones and combination bands.

Qualitative information is gained by the location of the absorption bands. Assuming that two atoms, causing an absorption band, behave as a classical harmonic oscillator, one can describe the frequency as follows [12, 13]:

$$\nu = \frac{1}{2\pi}\sqrt{\frac{k}{\mu}} \qquad (1.1)$$

Here, ν is the frequency, k the force constant and μ the reduced mass, given by

$$\mu = \frac{m_A m_B}{m_A + m_B} \qquad (1.2)$$

Although the model is based on classical mechanics, one can easily see that the frequency depends on the masses of the involved atoms (μ) and the force constant of the involved bonds (single-, double-, triple-bond).

Beside chemical identification, quantification is possible as well. Therefore, the Beer-Lambert law has to be applied:

$$A_{(\lambda)} = -\log \frac{I_{(\lambda)}}{I_{0,(\lambda)}} = \epsilon_{(\lambda)}\, c\, l \qquad (1.3)$$

The absorbance $A_{(\lambda)}$ caused by a substance is proportional to its absorption coefficient $\epsilon_{(\lambda)}$ at a certain wavelength λ, its concentration c and the pathlength l. It is calculated by the negative logarithm of the ratio between the detected intensity with the sample $I_{(\lambda)}$ and the light intensity of the background $I_{0,(\lambda)}$ (eq. (1.3), [14, 15]).

1.3.1. FTIR-Spectrometer

In the beginning of infrared spectroscopy, measurements were typically performed with prism- and grating-based spectrometers [16]. However, when quantitative anal-

ysis became more and more important, these dispersive spectrometers showed limitations in terms of stability, resolution and precision. By implementing an interferometer such as the most commonly applied Michelson interferometer, these limitations are circumvented. This development of instrumentation was made possible in the 60-70ties of the last century, as enough computer power for rapid calculation of the Fourier transformation was finally available.

The basic principle of a Michelson interferometer based Fourier transform infrared (FTIR) spectrometer [12, 14, 17] is as follows: IR radiation is emitted by a thermal source and collimated. Depending on the sample to be measured and the required resolution, an aperture can be installed in the optical beam. Then, a beam splitter splits the light into two directions whereas one beam is reflected at a fixed mirror and the other one at a moveable mirror (see fig. 1.2). The beams interfere again at the beam splitter and, by dislocating the moveable mirror, an interferogram can be recorded at the detector. A crucial part in this setup is the HeNe-laser which is also passing the interferometer. It delivers the position of the movable mirror at extremely high precision. Using the Fourier transformation, the interferogram is converted into a spectrum.

However, three advantages of the FTIR spectrometer over grating based spectrometer can be summed up [17]:

Multiplex advantage (Fellgett): Instead of measuring each frequency subsequently, all wavelengths are simultaneously detected.
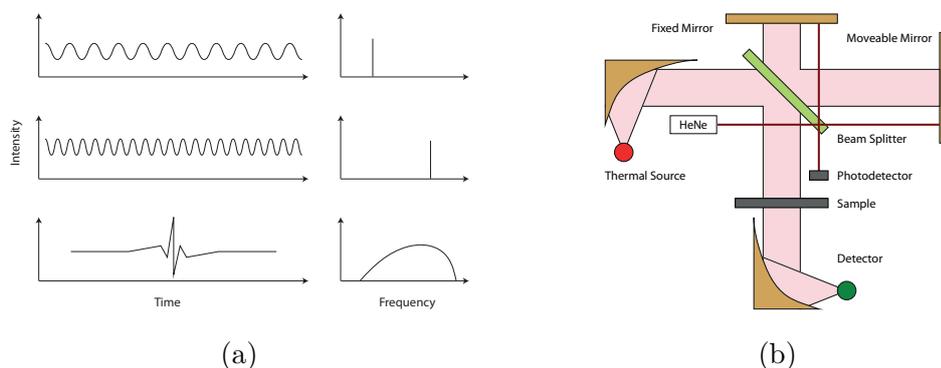
Figure 1.2.: (a): Examples of signals in the time- and frequency-domain. The mathematic relation between them is the Fourier transformation. (b): Simplified scheme of an FTIR spectrometer based on a Michelson interferometer.

Throughput advantage (Jacquinot): Dispersive spectrometers require a narrow slit to gain a proper resolution. This can be avoided by applying an interferometer which results in increased light intensity at the detector.

Wavelength precision advantage (Connes): The position of the moving mirror in the interferometer is determined by a HeNe-laser. Its much higher frequency and its narrow transition at 632.8 nm allows precise localization of the mirror and enables simultaneous calibration of the wavelength axis of the MIR spectrum during acquisition of the IR-interferogram. This, in combination with large optical path differences, also allows a higher spectral resolution compared to dispersive spectrometers.

1.3.2. Infrared Sources

Blackbody Radiation

Conventional IR spectrometers are usually based on broadband emitting sources such as the Globar (made out of SiC) or the Nernst glower (ceramic based on ZrO_2). Their basic principle is the black body radiation which is described by Planck's law [18]:

$$L_\sigma(\tilde{\nu}, T) = 2 \times 10^7 hc^2 \tilde{\nu}^3 \frac{1}{e^{\frac{100hc\tilde{\nu}}{k_B T}} - 1} \tag{1.4}$$

In eq. (1.4), L_σ represents the spectral radiance, h the Planck constant, T the absolute temperature, k_B the Boltzmann constant, $\tilde{\nu}$ the wavenumber and c the speed of light. It is obvious that the emitted radiation at a certain wavelength is strongly temperature-dependent (see fig. 1.3). To achieve a usable intensity, these IR sources are typically operated at temperatures above $1000\,°C$ (Globar: $\sim 1000\,°C$, Nernst glower: $\sim 2000\,°C$). Even higher temperatures would not improve the situation, as the maximum emission shifts towards smaller wavelength. However, the resulting output power is in the range of milliwatts ($\mu W/cm^{-1}$) and requires a proper spectrometer design to achieve usable spectra.

Synchrotron

Another IR source is the synchrotron. Electrons are accelerated in an pre-accelerator to relativistic speed and injected into the storage ring, where their energy can be
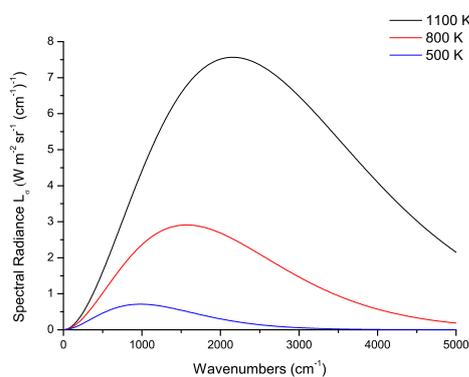
Figure 1.3.: Spectral radiance of a black body at different temperatures calculated with eq. (1.4).

further increased. The circulating in the storage ring goes along with a change in direction which is equal to an acceleration. The result is the emission of radiation and the emitted wavelength depends on the energy of the electrons. It can cover the whole electromagnetic spectrum from the FIR up to x-rays. In comparison to thermal IR sources, the emitted radiation is highly collimated and shows a much higher brightness as shown in fig. 1.4. The main disadvantage of such an IR source is its size and the costs of the infrastructure. The typical diameter of a storage ring is in the range of several tens of meters which makes it virtually impossible to apply it for every-day IR spectroscopy or even to process analytics.
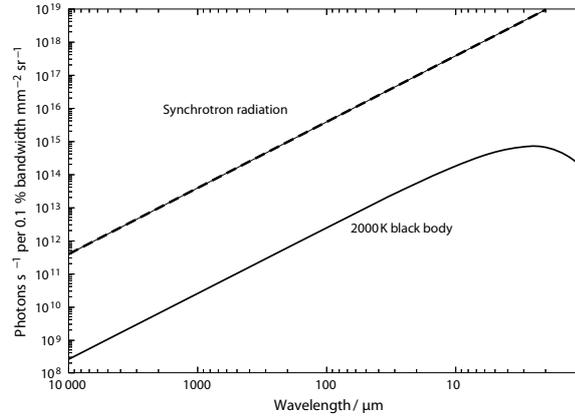
Figure 1.4.: Comparison of the brightness of a synchrotron source and a blackbody emitter at 2000 K, [19, 20]

.

1.4. Quantum Cascade Laser

Conventional semiconductor lasers work in the way that charge-carriers, namely electrons and holes, recombine at the interface of materials with different energy levels. The result of this recombination is the emission of a photon with the energy equal to the band gap of the materials (fig. 1.5a). As the band gap is material dependent, the material system has to be changed if a different wavelength is desired. Typical semiconductor materials are, for example, silicon (Si, 1.1 eV), gallium arsenide (GaAs, 1.43 eV) and gallium nitride (GaN, 3.4 eV) [21].

Lasers which emit in the MIR-region and rely on the recombination of electrons and holes are based on lead salts. These are, for example, PbS, PbSe, PbTe and PbSnSe whereas their band gap is in the range of 0.07–0.41 eV (corresponds to 3–20 µm) [22]. Single mode operation is achieved by integrating either a distributed feedback (DFB)-

grating or a distributed Bragg reflector (DBR) [23] and maximum temperatures for pulsed and continous wave operation are $85\,°C$ and $-100\,°C$, respectively.

Although the output power of lead salt lasers is in the milliwatt-range, their efficiency is limited. A much more efficient way to generate photons in the MIR-region is the quantum cascade laser (QCL). Hereby, the light generation takes place in defined quantum wells of a semiconductor. These quantum wells (fig. 1.5b) can be designed and are the result of material layers with defined thickness. The first functional devices were presented in 1994 by Faist et al. [24].

Beside the highly efficient light generation, the emitted spectrum of a QCL is, compared to a Globar, very sharp. This property relies on the cavity, which amplifies only certain wavelengths. Using an appropriate laser cavity design, a spectral linewidth of less than $0.001\,\mathrm{cm}^{-1}$ can be achieved. This is the main feature for IR-spectroscopy as the number of mechanical parts can be reduced (no interferometer) to measure the absorption at a certain wavelength. Other mentionable advantages are the small size, the coherent radiation, the inherent polarization and the high modulation depth in amplitude (up to the gigahertz-range).

1.4.1. Gain Medium

The above mentioned alternating semiconductor layers build up the quantum cascade structure and an example is shown in fig. 1.6. The thickness of each layer influences the energy levels and thus the emitted wavelength. One can distinguish two different sections, namely the active and the injector region. The active region is responsible
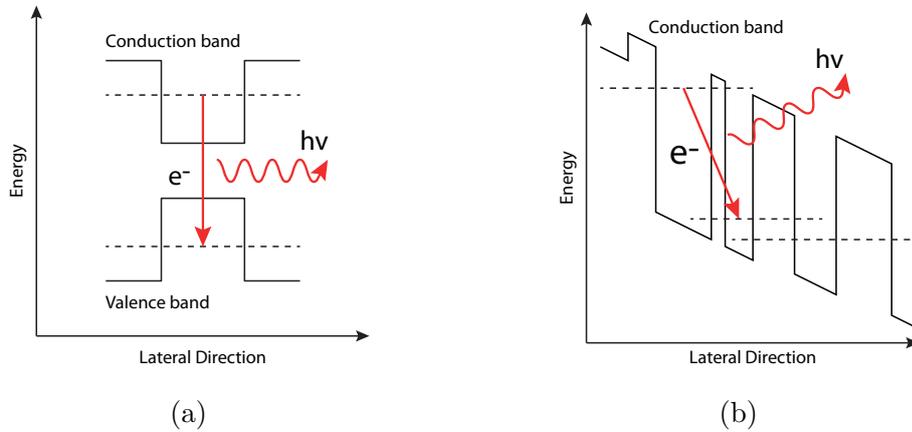
(a) (b)

Figure 1.5.: Basic principle of the light generation in a typical semiconductor laser (a) and a QCL (b). The first one is based on interband transitions (recombination of an electron and a hole), while the second one uses intersubband transitions for light generation.

for the light generation. Different active region designs are available (three-well [24], superlattice [25], bound-to-continuum [26]). The injector extracts the electrons from the lower laser state and fills the upper lasing level of the following period (see fig. 1.6).

It has to be noted that this type of photon-emission allows the re-use of electrons as no electron/hole-recombinations occur. Hence, the optical power can be increased by repeating the quantum cascade without increasing the current [28]. The result is a photon/electron ratio of > 1, compared to a ratio of 1 obtained with conventional semiconductor lasers.

After simulating and optimizing the nano structure with sophisticated software (for instance [29–31]), the semiconductor material is grown. Two technologies are there-
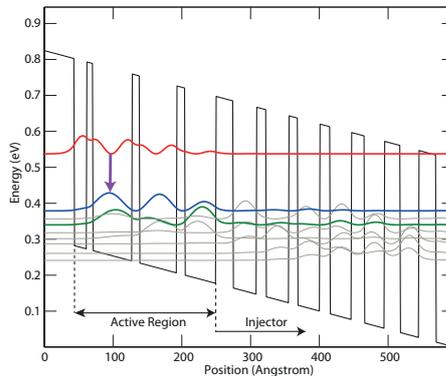
Figure 1.6.: Example of a quantum cascade with calculated energy levels (structure: P51 [27], material: InGaAs/InAlAs, $51\,\mathrm{kV\,cm^{-1}}$). Red→Blue: levels for light emission. Green: depopulation of lower laser level.

fore available: the molecular beam epitaxy (MBE) and the metalorganic vapor phase epitaxy (MOVPE). For MBE, a substrate wafer is transferred into a ultra high vacuum chamber equipped with heatable effusion cells [32–35]. These effusion cells are filled with the source materials, such as Ga or In. Heating the cells lets the material evaporate and deposit on the substrate wafer. A shutter opens/closes the flux from the individual cells to the sample in order to control the material composition. The growth rate is in the range of one monolayer per second and manufacturing a single QCL-wafer typically takes several hours. MOVPE, also known as metalorganic chemical vapor deposition (MOCVD), is in contrast a chemical process where metalorganic precursors (e.g. TMAl, TMIn) or hydrides (e.g. AsH_3, PH_3) are decomposed at the surface of the substrate wafer [36]. The advantage of this technology is that it can be operated at moderate pressures (10–760 torr) and allows a higher growth rate (1–$5\,\mathrm{\mu m\,h^{-1}}$) [37]. However, the higher rate is accompanied by increased

impurities due to the generated by-products and the toxicity of the precursors has to be considered [38].

The active core, consisting of periodic repetitions of the active and injector region, is located between the substrate wafer and cladding layers. As the refractive index of the enclosing layers is lower than that of the active zone, the light is guided due to total internal reflections. The difference of the refractive indexes can be artificially increased by embedding the active zone in a thin layer of higher refractive index. An example of such a lateral confinement is shown in fig. 1.7 whereas the overlap of the guided mode and the active zone is referred to as confinement factor Γ:

$$\Gamma = \frac{\int_{act} |E|^2 \, dz}{\int_{-\infty}^{\infty} |E|^2 \, dz} \tag{1.5}$$

Here, E is the transverse electromagnetic field distribution and z the growth direction. To put it in practical terms, the active core layer is at the same time gain medium and waveguide.
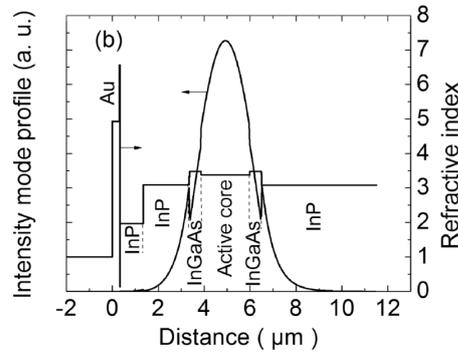

Figure 1.7.: Lateral mode distribution and refractive index of the laser material P51 [27].

1.4.2. Resonator

Generating the light is the first step in building a laser. Another requirement is the amplification of the radiation which is achieved by a resonator. Several approaches are available and the most important ones are discussed in the following subsections:

Fabry Perot Cavity

The Fabry-Perot (FP) cavity is the simplest way to build a resonator. It uses the edges of a laser as semi reflective mirrors and the emitted wavelength depends on the laser's cavity length. The amplification of the light requires a standing wave which is calculated using the equation

$$m\frac{\lambda}{2} = n_{eff}L \tag{1.6}$$

whereas m is an integer > 0, λ the wavelength, n_{eff} the effective refractive index and L the cavity length. The losses can be summed up as follows:

$$\alpha_{total} = \alpha_{waveguide} + \alpha_{mirror} \tag{1.7}$$

Due to the physical boundaries of the FP-design (fig. 1.8), the laser emits different wavelengths at the same time. Tunability is given by changing the cavity length (thermal expansion of the material) and the refractive index (also temperature dependent). Therefore, external heating of the device changes the emitted wavelength. The same effect is observed when the pulse length or the repetition rate are increased or an additional bias current is applied. As the practical thermal operation range of a

QCL is limited, the emitted wavelength can only be influenced by a few wavenumbers. Moreover, the emission of different modes at the same time reduces the applicability in IR-spectroscopy, where a certain spectral resolution is required.

(a) Lateral view

(b) Top view

Figure 1.8.: Simplified structure of a QCL with FP cavity.

External Cavity

An alternative approach to fulfill the resonance condition is to mount a diffraction grating at one end of the laser bar (fig. 1.9) [39–43]. Such an external cavity - quantum cascade laser (EC-QCL) can be tuned over several hundreds of wavenumbers (depending on the gain medium) [44]. Two mechanical configurations, namely the Littrow- and the Littman-configuration [45, 46], are available.

Due to the required optical grating, the losses increase as follows:

$$\alpha_{total} = \alpha_{waveguide} + \alpha_{mirror} + \alpha_{externalgrating} \tag{1.8}$$
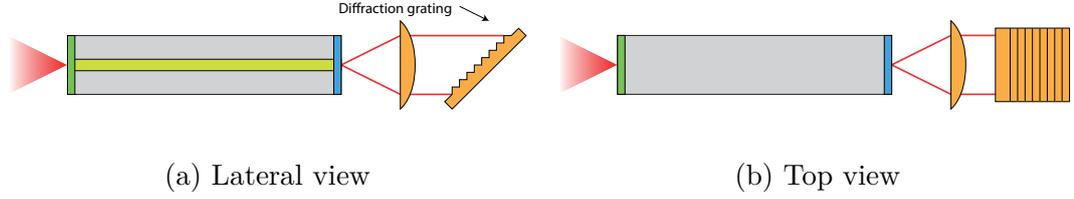
(a) Lateral view   (b) Top view

Figure 1.9.: Basic scheme of an EC-QCL with Littrow-configuration, enabling the emission of a single wavelength.

Distributed Feedback Cavity

The DFB cavity [47] is an improvement of the FP cavity whereas a diffraction grating is etched directly into the top layer of the device (fig. 1.10). This modification suppresses unwanted frequencies and allows the emission of a single wavelength. Subsequently, they are perfectly suited for quantification of small molecules in the gas phase as they show many extremely sharp ro-vibrational absorption lines. The period Λ of the grating is calculated using eq. (1.9):

$$\Lambda = \frac{m\lambda}{2n_{eff}} \tag{1.9}$$

whereas m stands for the order of the grating. For $m = 1$, emission occurs only at the facets of the device. In contrast, a second order grating allows light extraction through the top (surface emission) and the bottom (substrate emission) of the waveguide as well. The resulting losses are

$$\alpha_{total} = \alpha_{waveguide} + \alpha_{mirror} + \alpha_{grating} \tag{1.10}$$

The emitted wavelength depends mainly on the grating periodicity and can be tuned, like an FP cavity based QCL, by altering the temperature of the device.

(a) Lateral view

(b) Top view

Figure 1.10.: Geometrical scheme of a DFB whereas the grating on top of the device allows single mode emission.

Ring-Cavity

The ring-cavity surface emitting laser (ring-CSEL) [48] is a special type of a DFB laser. The circular shape of the waveguide is basically a ridge laser with (theoretically) infinite length (fig. 1.11). Due to the absence of facets, the light has to be extracted through the surface or the substrate which is realized with a second order grating. The occurring losses can be calculated as followed:

$$\alpha_{total} = \alpha_{waveguide} + \alpha_{substrate} + \alpha_{surface} + \alpha_{grating} \tag{1.11}$$

(a) Lateral view

(b) Top view

Figure 1.11.: Basic structure of a ring-CSEL. Surface/substrate emission is achieved by a second order grating.

While FP- and DFB-QCLs have a beam divergence in the range of 40–50° (e.g. [49, 50]), ring-CSELs show a much lower one (single-mode emission: ∼3°, multi-mode emission: ∼10°, [51]). This feature could lead to much smaller sensors as the number of optical elements can be reduced. The production of arrays is possible as well and such a device can be seen in fig. 1.12. Although the manufacturing process is similar to DFB-QCLs, ring-CSELs are still research devices and not yet commercially available.
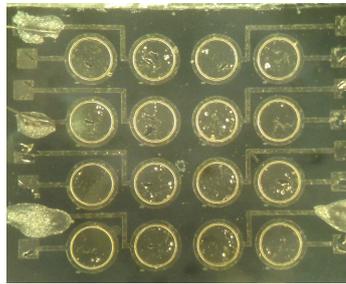
Figure 1.12.: Picture of a cleaved wafer with 16 individual ring-CSELs.

1.4.3. Commercial Availability of Quantum Cascade Lasers

A list of current companies manufacturing QCLs and their cavity types can be found in table 1.1.

Manufacturer	FP	EC	DFB
III-V Lab	✓		✓
Alpes Lasers	✓		✓
AdTech Optics	✓		✓
Block Engineering		✓	
Daylight Solutions		✓	
Hamamatsu			✓
Laser Components			✓
Thorlabs	✓		✓
Nanoplus	✓		✓
Pendar Technologies			✓
Pranalytica		✓	

Table 1.1.: Overview of QCL manufacturers and the available cavity types.

Chapter 2.

Materials and Methods

2.1. PATOV-Sensor

The central part of the PATOV-Sensor was the optical setup, which allowed to monitor the cleaning processes. The key elements were a tunable EC-QCL, a custom built flow cell and a detector. However, a liquid handling system had to be installed as well to transport the liquid to be analyzed to the flow cell. Additional requirements of the liquid handling system were loading calibration samples into the flow cell and flushing it with cleaning agents to prevent fouling of the windows. Finally, all components had to be assembled in a transportable housing in order to enable on-site measurements at different test plants. The necessary parts are described in the following subsections.

2.1.1. Optical and Electronic System

EC-QCL

The EC-QCL (Daylight Solutions (CA, USA), purchased in 2009) has already been characterized in [52, 53]. Detailed information about the device is available in [54] and therefore only the most important facts concerning the EC-QCL are listed here.

As in most cases the space on an optical breadboard is limited - therefore Daylight Solutions split the EC-QCL into two parts: the laser driver and the laser head.

Operating the EC-QCL required electronics for generating the pulses, monitoring and setting the device's temperature and tuning the emitted wavelength. All these features were integrated in the laser driver which is shown in fig. 2.1a and fig. 2.1b. Connectivity to a computer was realized by an USB, GPIB and an RS-232 interface on the backside. Beside the data connections, five BNC connectors were available, whereas their purpose is listed in table 2.1.

Connector	Purpose
Trigger	Trigger output for monitoring the QCL pulses
Aux 1	Scan enable
Aux 2	Direction
Aux 3	Not connected
Aux 4	Not connected

Table 2.1.: List of the BNC connectors available at the back of the laser driver.
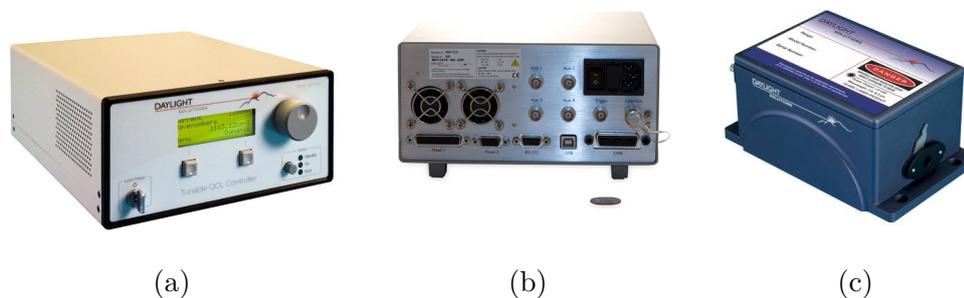
Figure 2.1.: EC-QCL from Daylight Solutions, Inc. (a), (b): laser driver, (c): laser head.

Although it was possible to control the EC-QCL via the front panel of the laser driver, it was more convenient to connect a computer using an RS-232 cable and to set the parameters remotely. For that purpose a program, part of the project Advanced Total Lab Automation Software (ATLAS) [55], was developed and the parameters (and the allowed values) that could be modified are listed in table 2.2.

The laser head (fig. 2.1c), containing the EC-QCL, was connected to the laser driver using a proprietary cable. The grating of the EC-QCL was tilted by a stepper motor, whereas the resulting spectral precision was $\sim 0.5\,\mathrm{cm}^{-1}$. Moreover, the device supported a scan-mode in which the grating was rotated with a defined speed. If the start- and stop-positions were kept constant over multiple scans, the temporal emission behavior would remain reproducible. The advantage of this method was that it was possible to record the spectrum of an analyte within a few seconds (tuning over the range of 1030–$1230\,\mathrm{cm}^{-1}$ took $1.2\,\mathrm{s}$). A time-resolved spectral characterization of the scan-mode is shown in fig. 2.2. Details of the employed measurement method

Parameter	Range of values
Pulse frequency	4.7–100 kHz
Pulse width	40–500 ns
Current	0–1700 mA
Emitted wavelength (= tuning range)	1024–1230 cm^{-1}
Scan speed	1–6 µsteps (6 µsteps correspond to 1.2 s tuning time over whole spectral range)
Scan repetitions	1–100 000

Table 2.2.: Allowed operation parameters of the EC-QCL.

and additional information can be found in [52].

Flow Cell

The utilized flow cell (shown in fig. 2.3) was based on two rectangular-shaped CaF_2 windows (38x19x2 mm^3) which were separated by a 165 µm thick polytetrafluorethylene (PTFE) spacer. The purpose of the spacer was to build up a channel from the inlet to the outlet, allowing the transport of the sample, and it ensured a constant thickness which is required by the Beer-Lambert law. A constant temperature in the flow cell was realized by a cooling/heating system based on a Peltier element.
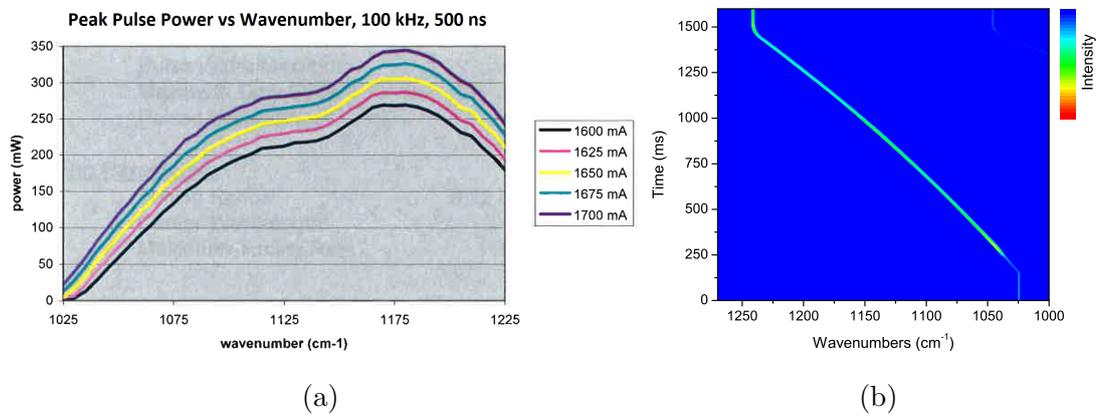
(a) (b)

Figure 2.2.: (a): Optical output power of the EC-QCL depending on the injection current and the set wavelength [56]. (b): Time-resolved characterization of the scan-mode (1030–1230 cm^{-1}).
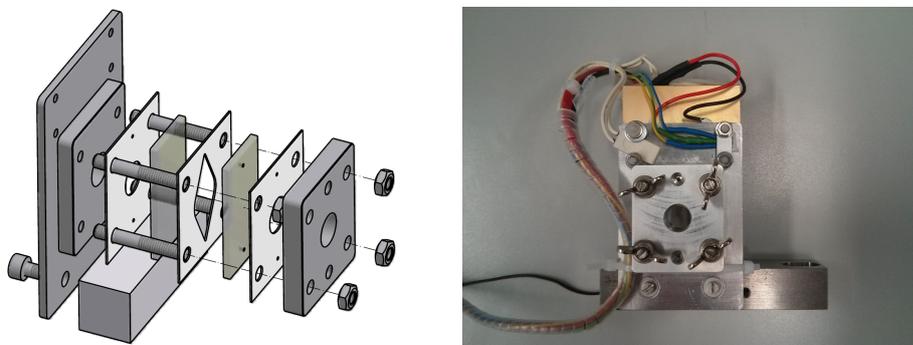

Figure 2.3.: Custom built flow cell with a Peltier element for thermostatization.

IR Detector

A mercury cadmium telluride (MCT) detector (OE-MCT-9-TE3-0.25, InfraRed Associates, FL, USA) was used for sensing the infrared radiation. While MCT detectors are frequently cooled with liquid nitrogen, this one was equipped with a thermoelectric cooling (TEC) element and operated at $-58\,°C$. Although the noise increases with the temperature, a TEC-MCT detector is much more practical as it is independent from a liquid nitrogen supply. The detector-element was equipped with a parabolic reflector and packaged in a TO-66 case.

Controller Board WT

The Controller Board WT was an in-house developed device for operating the IR detector and converting the pulsed detector signal into a direct current (DC) signal.

The detected laser pulses were converted into a DC signal using the boxcar integrator technology [57]. It basically consists of three parts – the input amplifier, the sample and hold element and a gate former. The gate former allows the user to define a subsection of the emitted pulse and controls the loading of a capacitor. The capacitor acts, together with the hold-element, as a low pass filter and the output can be digitized with a standard analog digital converter (ADC). A simplified circuit design is shown in fig. 2.4.

In addition, two temperature controller for stabilizing the temperature of the flow cell and the detector's case were available.
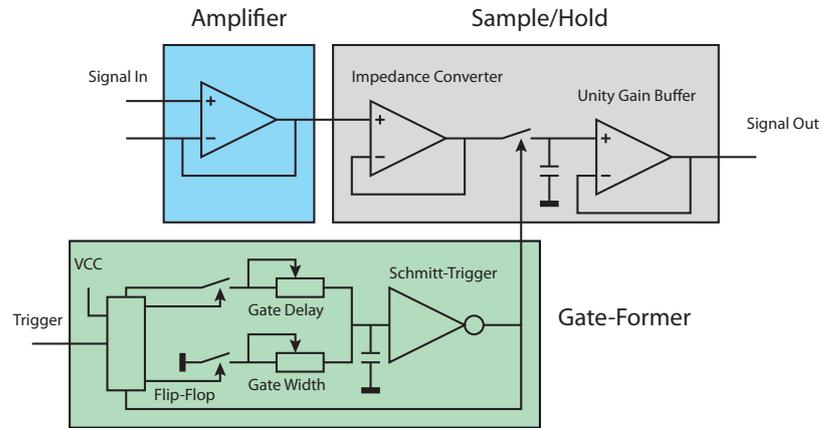
Figure 2.4.: Basic circuit design of a Boxcar Integrator [57, 58].

AD7760

The ADC AD7760 (Analog Devices, MA, USA) was utilized to convert the boxcar filtered signal and supports 24 bit resolution at 2.5 MSPS. Considering the spectral resolution and tuning rate of the EC-QCL, the internal decimation rate was set to 32. This reduced the sample rate to 78.125 kSPS and thus the memory usage of the controlling computer. Before the data was stored, the number of data-points was reduced whereas the algorithm depended on the type of experiment. In case of a single-wavelength measurement, data blocks were averaged (laboratory vessel: 15625 data points, industrial vessel: 78125 data points). For operating the EC-QCL in tuning mode, 92000 data-points were recorded and filtered with a customized Fourier transform algorithm. Subsequently, each spectrum consisted of 154 data-points.

2.1.2. Flow Management

The liquid handling system consisted of two segments which were the interface to the process stream and the flow injection analysis (FIA) system. They were responsible for transporting the liquid samples from either the process stream or calibration vials into the flow cell.

Sensor Interface

If the PATOV-Sensor was operated as an online sensor, a gear pump (Verdergear VG1000, Verder B.V., Netherlands) transported the waste water continuously to a T-connector. One end was then attached to the FIA system of the sensor and the other one was connected to a control valve. Closing this valve reduced the flow to the drain and the liquid was directed to the flow cell of the sensor.
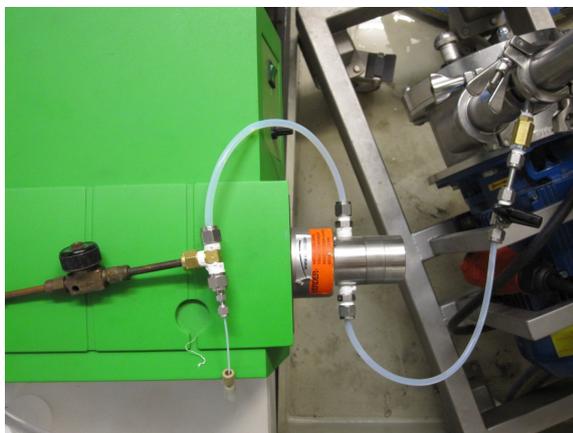

Figure 2.5.: Interface between the process stream and the PATOV-Sensor.

The optimal settings for the valve and the gear pump were evaluated by preparing two beakers whereas one was filled with tap water and the other one with a solution of glycerol ($\sim 1.5\,\mathrm{g\,L^{-1}}$) and water. After setting the pump speed and the valve position, the PATOV-Sensor was started and recorded the absorption at $1113\,\mathrm{cm^{-1}}$. The response time was identified by moving the suction hose from beaker A to B and measuring the time until a change of absorption was detected.

Flow Injection Analysis System

The second segment of the flow management was a FIA system. It consisted of an injection valve, a selection valve (VICI AG, Switzerland) and a syringe pump (XP 3000, Cavro Scientific Instruments, CA, USA).

When a cleaning process was monitored, the injection valve was in its default position *A*. The sample was directed to the flow cell and finally transported to a waste bottle.

Depending on the chemicals in the pharmaceutical process, adsorption could occur on the walls of the tubes and especially on the windows of the flow cell. Major errors in the results were avoided by using chemically inert tubes made out of PTFE and repeated cleaning of the windows with ethanol or acetone. To do so, the syringe pump was used for loading the cleaning agent from the selection valve into a holding coil. By switching the injection valve to position *B*, the sample from the process stream was directed to the waste bottle and the fluid for cleaning was pumped from the holding coil to the flow cell. After flushing the flow cell, deposits from the

cleaning chemicals were removed by pumping high-purity water through the system. Moreover, calibration samples were injected into the flow cell in the same way and allowed automated calibration experiments.

2.1.3. Assembled PATOV-Sensor

As the PATOV-Project required the construction of a portable device, all components were assembled in a self built case based on aluminium profiles (Bosch Rexroth AG, Germany). Within the cage, two layers were used for housing the electronics and a third one was dedicated for the optical part and the FIA system. The construction is shown in fig. 2.6 and the connections between the devices can be seen in fig. 2.7.
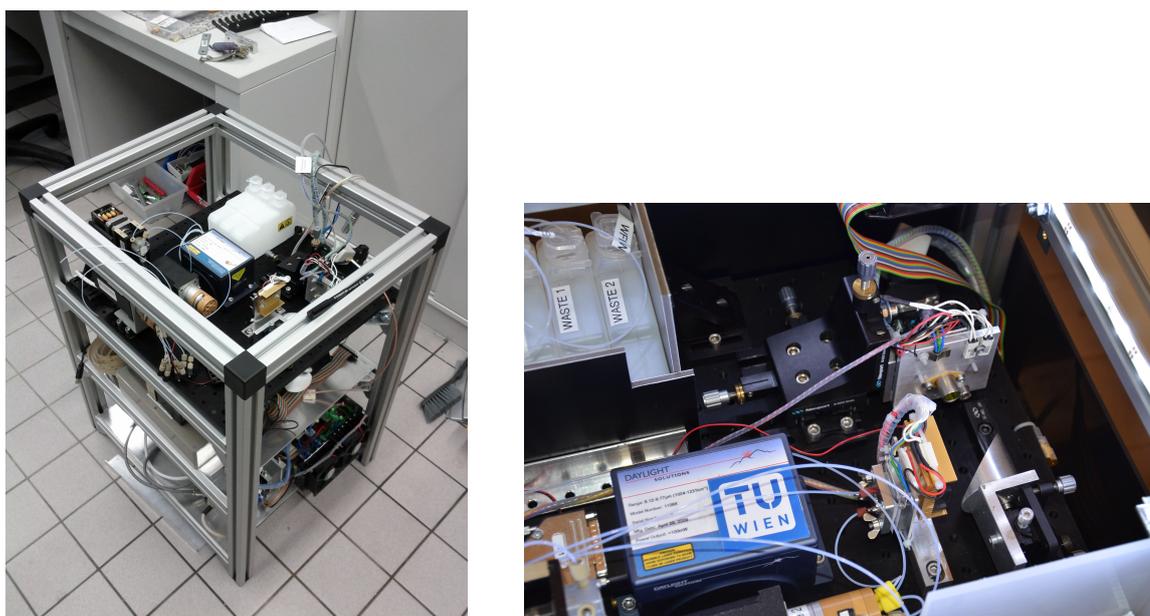
Figure 2.6.: PATOV-Sensor based on an EC-QCL.
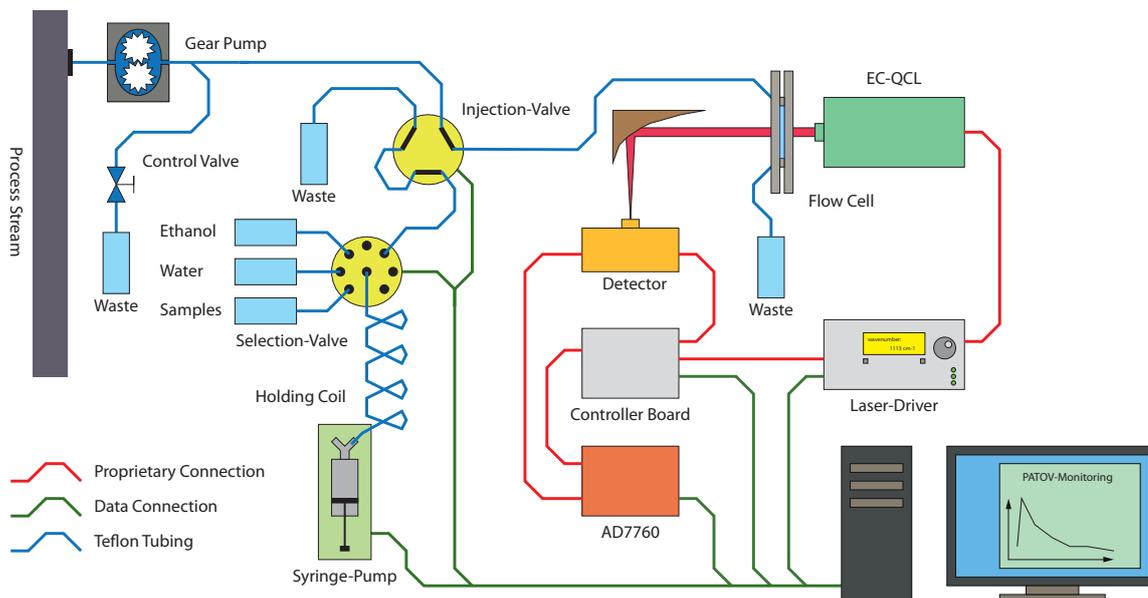
Figure 2.7.: Overview of the FIA system and the electronic connections of the PATOV-Sensor.

All electronic devices, except the gear pump, were connected to the computer by either an RS-232 or an USB connection and controlled by a custom developed software. The program was designed in LabVIEW 2009 (National Instruments, USA) as the required device drivers were available and easy to handle. While a state-machine-architecture [59] was used for continuously recording spectra, the cleaning of the CaF_2 windows with an ethanol solution was realized by a consumer-producer-architecture [60] and had to be initiated manually.

2.2. Investigated Analytes and Calibration Samples

The accessible concentration range as well as the linearity of the sensor were evaluated by recording calibration curves of glycerol and xanthan gum [61, 62]. Samples with known concentrations were prepared by weighing the analyte and the water used for diluting. A detailed list can be found in table 3.1 and table 3.2. The reduced number of samples of xanthan gum was owed to its low solubility. Spectra as well as the absorption values at $1113\,\mathrm{cm}^{-1}$ of these samples were measured.

Due to the fact that the TOC value is the established parameter in pharmaceutical community calibration curves use the weighed carbon content as x-axis. The conversion from $\mathrm{g\,L}^{-1}$ to TOC is calculated as follows:

Xanthan gum: One sub-unit: $C_{35}H_{49}O_{29} \rightarrow M_{Xanthangum} = 933.75\,\mathrm{g\,mol}^{-1}$
$1\,\mathrm{g} = 0.001\,08\,\mathrm{mol}$, Xanthan gum contains 35 carbon atoms $\rightarrow 0.0379\,\mathrm{mol}$ Carbon $\rightarrow$
$0.0379\,\mathrm{mol\,L}^{-1}\mathrm{x}12.07\,\mathrm{g\,mol}^{-1} = 0.454\,\mathrm{g\,L}^{-1}$ Carbon $= 454\,\mathrm{ppm}$

Glycerol: $C_3H_8O_3 \rightarrow M_{Glycerol} = 92.09\,\mathrm{g\,mol}^{-1}$
$1\,\mathrm{g} = 0.010\,85\,\mathrm{mol}$, Glycerol contains 3 carbon atoms $\rightarrow 0.0325\,\mathrm{mol}$ Carbon $\rightarrow$
$0.0325\,\mathrm{mol\,L}^{-1}\mathrm{x}12.07\,\mathrm{g\,mol}^{-1} = 0.392\,\mathrm{g\,L}^{-1}$ Carbon $= 392\,\mathrm{ppm}$

2.3. PATOV Test Plants

The applicability of the PATOV-Sensor was evaluated with three different test plants. The first one was designed for preliminary experiments with the EC-QCL based sensor. The second plant was similar to industrial scale, meeting the industrial requirements and could be applied in a real application. The third one was part of the research facility of the project partner CMC Biologics (Copenhagen) and usually applied for experimental fermentations.

2.3.1. Laboratory Vessel

The first experiments were performed in a small-scale laboratory vessel (fig. 2.8). Its relatively small volume of approximately $8\,\mathrm{L}$ made it perfectly suited for the first evaluation tests as less tracer substances and water were used. Due to the high throughput of the gear pump ($\sim 1\,\mathrm{L\,min^{-1}}$), which built the interface to the PATOV-Sensor, the drain of the gear pump was returned back into the vessel. The result was that the tracer substances accumulated and that it behaved similar to a continuously stirred-tank reactor. Moreover, the laboratory vessel was equipped with an agitator to gain fast homogenization and a valve at the bottom to drain the liquid.

Experiments with the PATOV-Sensor and the laboratory vessel were performed by weighing the amount of tap water, introduced into the vessel. The stirrer was set to $120\,\mathrm{rpm}$. In the next step, the gear pump, responsible for transporting the liquid to the sensor, was started ($1500\,\mathrm{rpm}$) and a background measurement was performed by the sensor. After waiting $\sim 30\,\mathrm{s}$, the liquid was step-wise spiked with the analytes
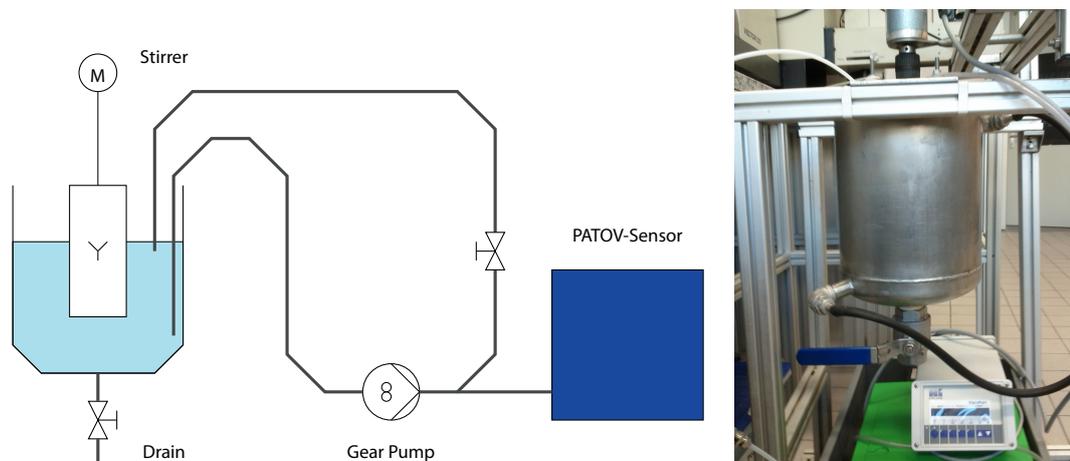
Figure 2.8.: Scheme and picture of the laboratory vessel.

whereas syringes ($1\,\text{mL}$ and $5\,\text{mL}$) were used for glycerol and a spattle for xanthan gum (exact mass determined by weighing).

At the end of each experiment, the glycerol (and xanthan gum) solution was substituted by fresh tap water to clean the vessel for the following spiking experiment. In addition, temporal stability could be validated if the absorption decreased back to $0\,\text{mAU}$.

2.3.2. Industrial Vessel with CIP-Equipment at the Vienna University of Technology

A second test plant was built for demonstrating the applicability of the PATOV-Sensor in industrial scale (fig. 2.9). Running a real pharmaceutical fermentation was not suited as it is time and resource consuming. Therefore it was decided to contaminate the walls of the vessel with the tracer substances manually. A water tank with a volume of $1000\,\mathrm{L}$ had to be filled with water. Tap water was used instead of WFI to reduce operation costs. A pump (pump 1), located at the bottom of the reservoir, transported the cleaning liquid to the spray ball at the top of the vessel to be cleaned. The water was then sprayed at the walls of the vessel and allowed the removal of residuals. To avoid filling of the vessel, the cleaning liquid was either pumped (pump 2) to the drain or back to the water reservoir. Similar to the laboratory vessel, recirculation of the water was the preferred operation mode as the minimum feed rates of the installed pumps were $2000\,\mathrm{kg\,h^{-1}}$. Moreover, two different spray balls were compared (Rensekugler and Sani Midget) and two different pump rates ($2000\,\mathrm{kg\,h^{-1}}$, $5000\,\mathrm{kg\,h^{-1}}$) were evaluated as well.

The gear pump feeding the PATOV-Sensor was attached to the setup next to pump 2 together with a valve for drawing offline samples.
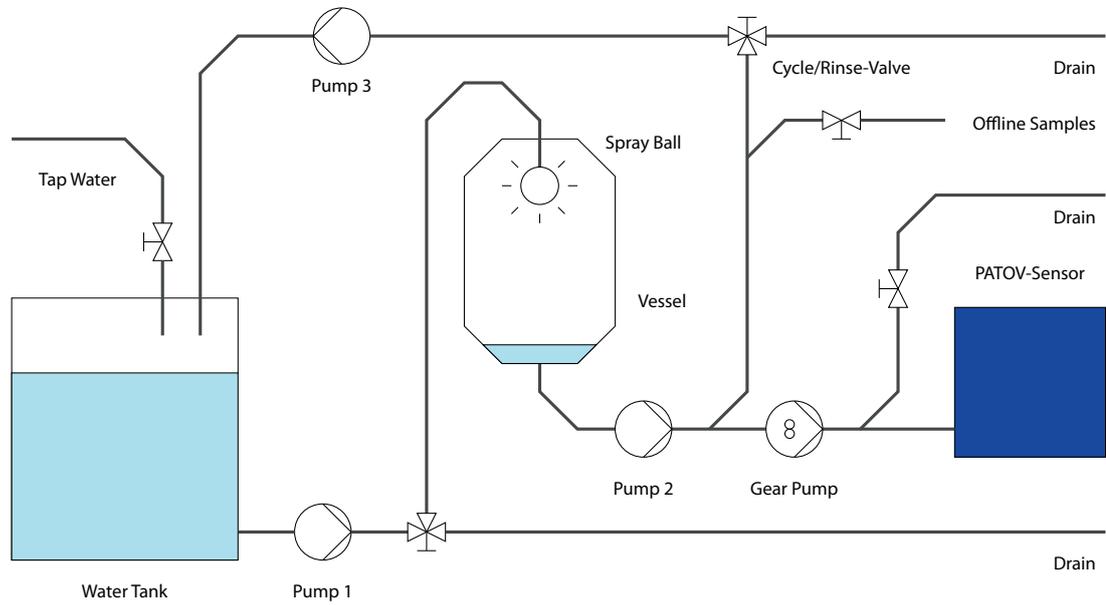
Figure 2.9.: Scheme and picture of the industrial sized PATOV plant.

2.3.3. Industrial Vessel with CIP-Equipment at CMC Biologics

The third test plant was located at the project partner CMC Biologics (Copenhagen). The vessel to be cleaned (Biostat D 100, Sartorius) was part of the research facility which made it necessary to redesign the CIP-equipment and also limited the number of experiments. Due to company regulations, only rinse experiments were allowed to avoid additional contamination of the laboratory equipment. The consequence was a smaller and manually operated CIP-system with less pumps, valves and hoses (a simplified scheme is shown in fig. 2.10). Moreover, the water tank was downsized to $700\,\mathrm{L}$ and the pump rate was reduced to $490\,\mathrm{kg\,h^{-1}}$ and $1370\,\mathrm{kg\,h^{-1}}$, depending on the experiment.

Figure 2.10.: Scheme of the CIP plant and picture of the vessel to be cleaned at CMC Biologics.

2.4. A New Laser for the Quantification of Proteins

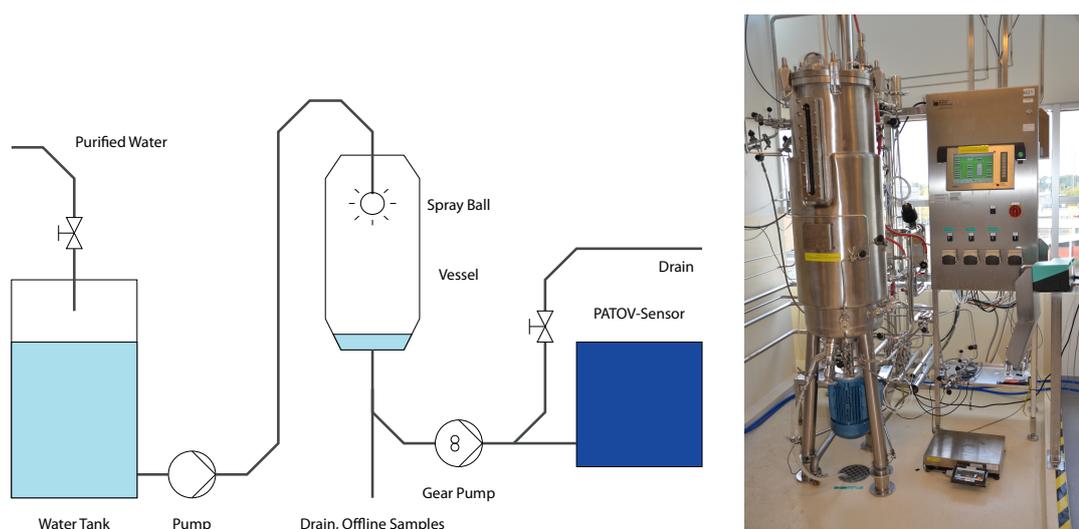The spectral coverage of the EC-QCL (1024–$1230\,\mathrm{cm}^{-1}$) is typical for carbohydrates. Proteins exhibit little absorption in that region but the absorption coefficient is much higher at the position of the amide I-band located near $1650\,\mathrm{cm}^{-1}$. This region is mainly dominated by the C=O stretching vibration [63]. Although proteins show reasonable absorption within this range, precise quantification is difficult since water and water vapor interfere with the measurement. While the strong temperature dependence of the absorption-coefficient of water can be circumvented in laboratory environments by precise temperature stabilization and flushing the experimental setup with dry air, it is impracticable for industrial environments. Another spectral range, where proteins absorb the IR radiation properly is that of the amid II-band located around $1550\,\mathrm{cm}^{-1}$.

An exemplary FTIR spectrum of soy protein is illustrated in fig. 2.11. One can clearly see the much stronger absorption in the amid-I and amid-II region than in the carbohydrate region.

Due to the fact that QCLs are still experimental semiconductor devices and not every wavelength is commercial available at sufficient power and spectral quality, a suiting laser for absorption measurements in the amid II range had to be developed.
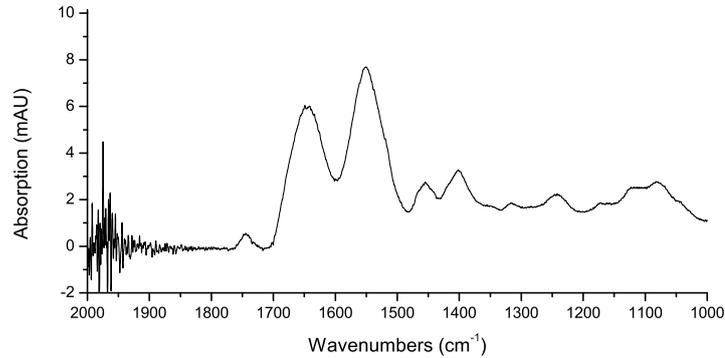
Figure 2.11.: FTIR spectrum (triple reflection ATR-element, background measurement with water) of soy protein ($40\,\mathrm{g\,L^{-1}}$).

2.4.1. Substrate H861

The substrate material for the ring-CSEL was designed and grown at the Institute for Solid State Electronics (Vienna University of Technology, Austria) and was a slightly modified version of the material presented in [64]. The active zone consisted of 35 periods of InAlAs/InGaAs and was embedded in an InGaAs sandwich. The top layers were 1500 nm and 800 nm InAlAs whereas the Si-doping levels were $1 \times 10^{17}\,\mathrm{cm^{-3}}$ and $2 \times 10^{17}\,\mathrm{cm^{-3}}$. The detailed growth sheet is listed in appendix B.3.

An additional feature of this band structure was that it worked both as a QCL and a quantum cascade detector (QCD), depending on the operating conditions (see fig. 2.12). At $58\,\mathrm{kV\,cm^{-1}}$, the quantum cascade acts like a typical QCL and emits light at $\sim 1470\text{--}1540\,\mathrm{cm^{-1}}$. If no voltage is applied, the active region absorbs light and generates an electrical current due to the optimized structure. This property will allow the development of miniature sensors as both, laser and detector, work at

room-temperature and support due to the quantum structure operation in the GHz range [65].
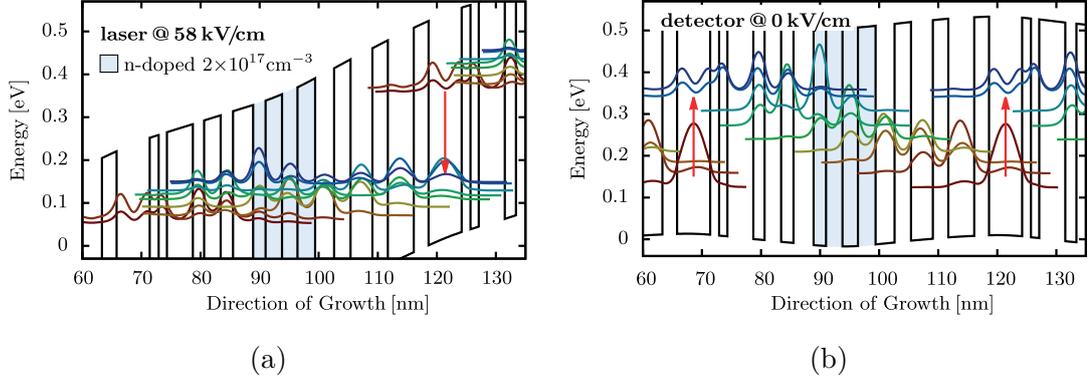
Figure 2.12.: Band diagrams of a QCL/QCD device at $58\,\mathrm{kV\,cm^{-1}}$ (laser, (a)) and $0\,\mathrm{kV\,cm^{-1}}$ (detector, (b)) [64]. The red arrow inicates the lasing transition and light absorption, respectively.

2.4.2. Processing

The ring-CSEL were built by applying the top-down-processing which uses different lithography, etching and deposition methods [48]. This production technique is very important for the semiconductor industry and can be adopted for a specific problem very easily. A detailed spec sheet with all device parameters is listed in appendix B.1 and a simplified sequence of the manufacturing steps is shown in appendix B.2.

The processing started with the removal of the oxide-layer on the substrate using diluted KOH. The calculated grating structures were transferred onto the sample by electron beam lithography. The simpler UV-lithography was not suitable because of

two reasons: Firstly, the grating structure was in the lower micrometer-range making it impossible to achieve sharp features with standard UV-lithography. Secondly, UV-lithography would require a new photo mask every time the grating periods of the ring-CSEL changes.

After spin-coating the substrate with poly(methyl methacrylate) (PMMA), the cleaved wafer was transferred into the e-line chamber, aligned and exposed to the electron beam which wrote the structure. The electron beam destroyed the molecular PMMA structure, that could be removed subsequently. A thin Ti/Au/Ni-layer was deposited and, by applying a lift off process, the grating mask remained. Using a reactive ion etching (RIE) process, the grating, enabling the wavelength selection, was then etched into the substrate.

As the dimensions of the waveguide were independent from the desired wavelength and substrate, UV-lithography using glass masks was the preferred method. Etching the waveguide structure was performed at $250\,°C$, which was unsuited for polymer resists. Therefore, a Si_3N_4 layer was deposited and converted into the mask, used for the actual waveguide-etching step. When the waveguide-etching was finished, the Si_3N_4 mask had to be removed in an additional step.

The following step included deposition Si_3N_4 as an insulation layer. It prevented the device from short-circuits between the substrate and the top contact, which would enable the electrons to bypass the active region. UV-lithography and RIE were applied to remove the insulation layer from gratings. This was necessary as it absorbs IR radiation.

The top contact was produced in a lift-off process. The sputtered Ti/Au layer had to be removed from the grating slits and from the gaps between the different rings located on the wafer. Finally, Indium was used to solder the wafer onto a Cu-mount and each laser was connected to a printed circuit board (PCB) using a Au-wire.

2.4.3. Processed Devices

The lasing material H861 was evaluated by processing ring-CSELs with different grating periods, covering the available gain range. The inner radius of the waveguide was set to 189.5 µm and the outer diameter to 200.5 µm which corresponds to a ridge laser with 11 µm width and 1225 µm length. The number of grating slits and their according grating periods are listed in appendix B.4 whereas an effective refractive index of 3.225 and room temperatrue (293 K) were assumed. Moreover, the duty cycle of the grating was selected to be 65 %, which led to a reasonable outcoupling of the light, according to [66].

For the processing, small samples ($\sim 10\,\text{mm} \times 10\,\text{mm}$) were cleaved from the wafer. Taking into account, that each ring-CSEL required an area of 600 µm × 600 µm and the occurrence of rims on the wafer, 12×9 lasers were typically written by the electron lithography.

2.4.4. Laser Characterization

QCLs are typically characterized by recording emission spectra and light intensity (L) - current (I) - voltage (V) (LIV) curves. Therefore, the sample was placed on a TEC cooled mounting ($20\,°C$) and the emitted radiation was collimated using a ZnSe lens. The beam was then coupled into the FTIR spectrometer Equinox 55 (Bruker Corporation, MA, USA) with a spectral resolution of $0.2\,cm^{-1}$. Emission spectra were recorded by pulsing a single laser at a repetition rate of $5\,kHz$ and a pulse width of $100\,ns$ whereas the laser driver AVL-2-B (Avtech Electrosystems Ltd., NY, USA) was used. In addition, the detector signal was analyzed with a lock-in amplifier (5210EC, Princeton Applied Research, TN, USA) to quantify the light intensity. An oscilloscope (TDS 3032B, Tektronix, Inc., OR, USA) recorded the voltage and the current at the laser to calculate the LIV curves.
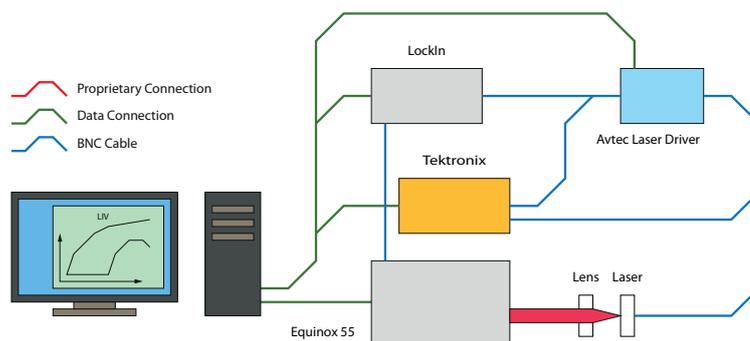
Figure 2.13.: Setup for recording LIV curves of the manufactured ring-CSELs.

Chapter 3.

Results and Discussion

3.1. Online Sensor

3.1.1. Spectra of the Tracer Substances

Spectra of the investigated tracer substances at different concentrations were recorded with the PATOV-Sensor and are shown in fig. 3.1b and fig. 3.2b. One can clearly see that glycerol has significant absorption bands at 1040 and $1120\,\mathrm{cm}^{-1}$ ($\mathrm{C-O}$ stretch, primary and secondary alcohol). Moreover, the molecule shows almost no absorption in the region 1150–$1190\,\mathrm{cm}^{-1}$. In contrast, xanthan gum absorbs between 1180 and $1030\,\mathrm{cm}^{-1}$ with an almost linear increase. Additional minor peaks can be identified at 1160, 1185 and at $1040\,\mathrm{cm}^{-1}$. The absorption bands are caused by the primary and

secondary alcohols (C−O stretch) which can be found in the sub-units of xanthan gum (glucose → backbone, mannose and glucaronic acid → side chain) [12].
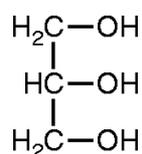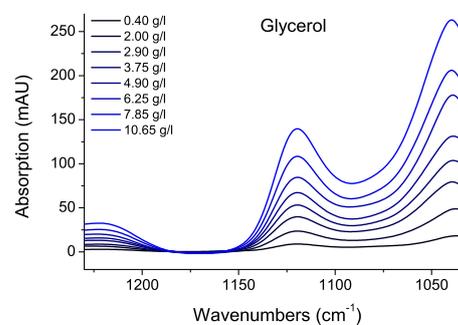
(a)   (b)

Figure 3.1.: Structure (a) [67] and spectra (b) of glycerol.
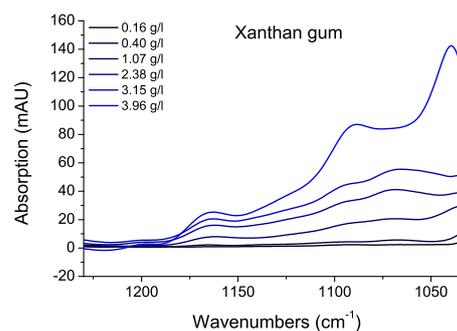
(a)   (b)

Figure 3.2.: Structure (a) [68] and spectra (b) of xanthan gum.

3.1.2. Linear Calibration Curves at 1113 cm^{-1}

The calibration curves for converting the measured absorption into a TOC value are shown in fig. 3.3. The wavelength of $1113\,\mathrm{cm}^{-1}$ was chosen as the EC-QCL emits

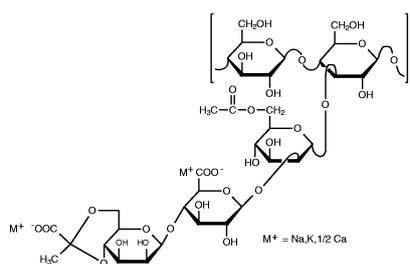| Sample	Glycerol (g)	Water (g)	Concentration $(\mathrm{g\,L^{-1}})$	TOC equivalent (ppm)	Absorption (mAU)
1	0.09	998.1	0.09	35	1.2
2	0.13	997.2	0.13	51	1.4
3	0.21	997.8	0.21	82	2.4
4	0.20	194.6	1.00	400	12.2
5	0.30	197.7	1.51	590	19.3
6	0.40	195.0	2.04	798	25.5
7	0.75	197.4	3.78	1476	48.6
8	1.25	193.7	6.41	2501	78.4
9	1.57	193.7	8.04	3136	100.6

Table 3.1.: Calibration samples of glycerol.

Sample	Xanthan Gum (g)	Water (g)	Concentration $(\mathrm{g\,L^{-1}})$	TOC equivalent (ppm)	Absorption (mAU)
1	0.04	252.7	0.16	72	1.2
2	0.10	250.9	0.40	180	2.6
3	0.27	252.4	1.07	485	8.5
4	0.49	252.0	1.94	881	15.5
5	0.60	251.9	2.39	1079	17.6
6	0.80	253.7	3.14	1427	24.3

Table 3.2.: Calibration samples of xanthan gum.

reasonable power for reliable measurements at this wavenumber and, in addition, both analytes absorb IR radiation at acceptable levels. The relevant parameters, namely the slope, intercept, R^2 and the LOD (calculated with the linear regression approach [69]) are listed in table 3.3.

(a) (b)
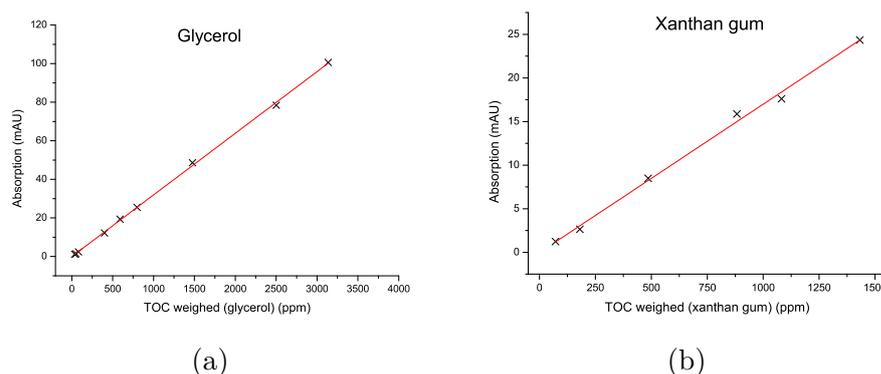
Figure 3.3.: Linear calibration curves of glycerol (a) and xanthan gum (b) at $1113\,\mathrm{cm}^{-1}$.

Parameter	Glycerol	Xanthan gum
Slope	$0.0320\,\mathrm{mAU/ppm}$	$0.0170\,\mathrm{mAU/ppm}$
Intercept	$-0.0247\,\mathrm{mAU}$	$-0.0315\,\mathrm{mAU}$
R^2	0.9995	0.9960
Limit of Detection	88.5 ppm	122.6 ppm

Table 3.3.: Calibration parameters and limit of detection calculated from the linear calibration of glycerol and xanthan gum.

3.1.3. Sensor Interface

The sample response curves used to determine the optimum settings of the control valve and the gear pump are shown in fig. 3.4. One can clearly see that the time delay essentially depends on the speed of the gear pump. If the valve is set to position 1/1, for example, and the gear pump operates at $500\,\text{rpm}$, the time delay is higher than $50\,\text{s}$. An increase of the speed of the gear pump to $1500\,\text{rpm}$ leads to a reduced delay of $\sim 10\,\text{s}$. By further closing the control valve, the sample flow rate to the PATOV sensor can be increased and the delay time optimized as well. While the responses at $1500\,\text{rpm}$ and the valve settings 1/4 and 1/8 are almost identical, it was decided to perform all measurements with setting 1/4 to avoid excess pressures at the windows of the flow cell. Therefore, the time delay caused by the sensor interface is approximately $6\,\text{s}$ (gear pump: $1013\,\text{mL/min}$).
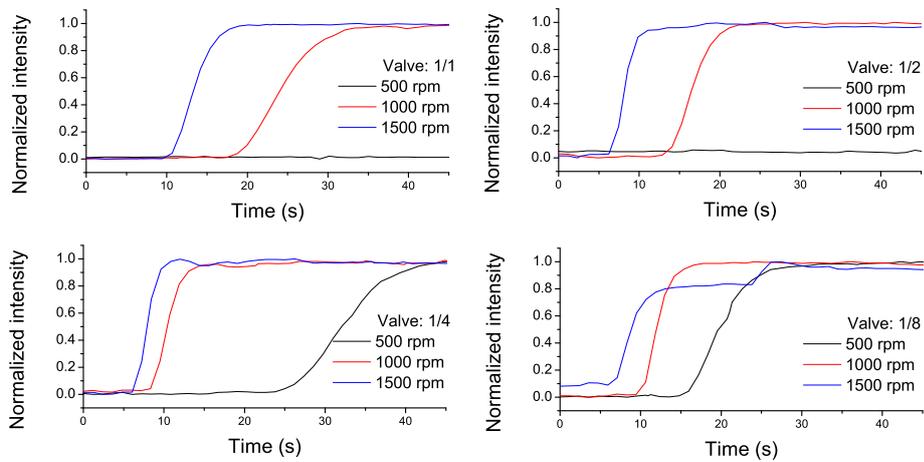
Figure 3.4.: Response time of the sensor interface at different control valve and gear pump parameters.

3.1.4. Laboratory Vessel

Glycerol

The results from the spiking experiments are plotted in fig. 3.5. Figure 3.5a contains the data gained by adding $5\,\text{mL}$ of glycerol in a step wise procedure and operating the PATOV-Sensor at $1113\,\text{cm}^{-1}$. The inset illustrates the fast response of the EC-QCL based sensor. The addition of the tracer substance is indicated by the blue arrows. At the end of the experiment ($t \sim 3800\,\text{s}$), the glycerol solution was was replaced with fresh tap water. As this was done in two steps, the absorption was first reduced to $\sim 150\,\text{mAU}$ for $\sim 200\,\text{s}$ before it went to $\sim 0\,\text{mAU}$ (at $t \sim 4100\,\text{s}$).

This experiment was repeated by adding $1\,\text{mL}$ per step and the resulting curve can be seen in fig. 3.5b.

(a) (b)
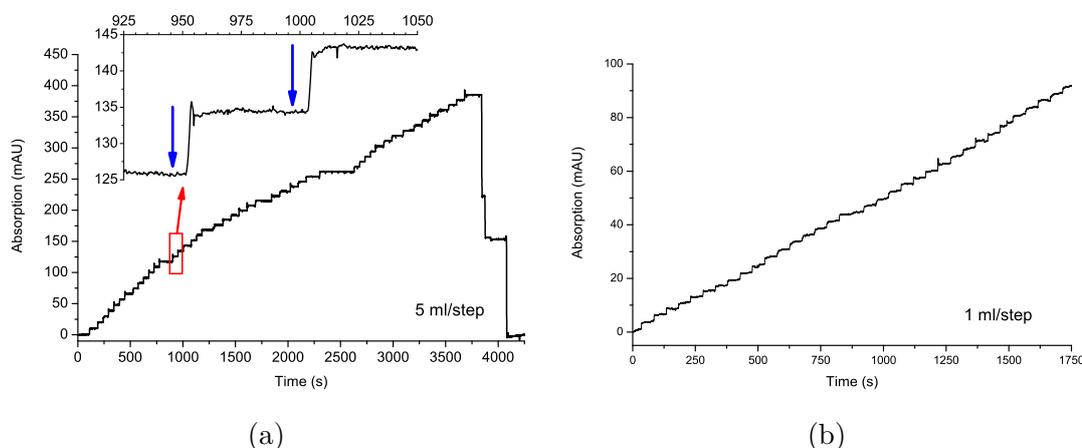
Figure 3.5.: Spiking the laboratory vessel multiple times with (a): $5\,\text{mL}$ and (b): $1\,\text{mL}$ glycerol per step.

As the water was weighed before it was placed in the laboratory vessel (7960 g), one can use these spiking experiments to create a linear calibration curve. To do so, the absorption data of the first eleven steps from fig. 3.5a were extracted and plotted against the carbon content of the added glycerol (fig. 3.6). Again, the relevant parameters (slope, intercept, R^2 and the LOD) were calculated and listed in table 3.4. By comparing the results of table 3.4 with table 3.3, one can see that the spiking experiments lead to a higher R^2 value and the LOD is almost 30% better.
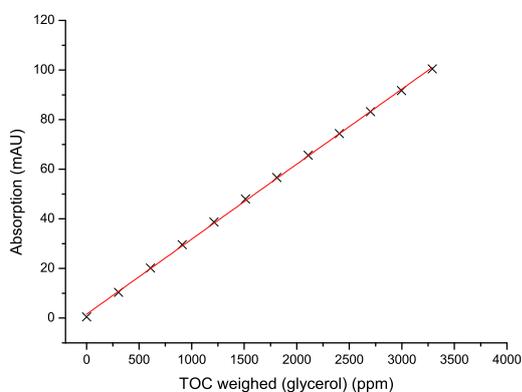
Figure 3.6.: Calibration curve gained by spiking the laboratory vessel.

Parameter	Glycerol
Slope	0.0302 mAU/ppm
Intercept	1.5529 mAU
R^2	0.9997
Limit of Detection	60.9 ppm

Table 3.4.: Relevant parameters of the linear calibration by spiking the laboratory vessel with glycerol.

Glycerol and Xanthan Gum

In addition to the spiking experiments where only glycerol was added to the water in the laboratory vessel, measurements with glycerol and xanthan gum were performed as well. In contrast to previous experiments, the PATOV-Sensor was operated in scan mode, which means that every $\sim 7\,\mathrm{s}$ a new spectrum in the range of 1030–1230 cm^{-1} was recorded. A detailed sequence how the analytes were added is listed in table 3.5.

The results are shown in fig. 3.7a. The two white lines indicate the wavelengths 1105 cm^{-1} and 1160 cm^{-1} which are extracted and plotted in detail in fig. 3.7b. One can see that the red curve shows more steps than the black one. This effect can be explained as glycerol absorbs IR radiation at 1105 cm^{-1} and is transmitting at 1160 cm^{-1} (see fig. 3.1b) resulting in a step in the red curve and a constant signal in the black one. In contrast, xanthan gum absorbs at both wavelengths (see fig. 3.2b), causing an increase in both curves. The negative peak at $t \sim 2800\,\mathrm{s}$ is the result of flushing the flow cell with an ethanol solution for proper cleaning.

At the end of the experiment, the liquid in the laboratory vessel was again replaced with tap water. While the absorption at 1105 cm^{-1} goes back to the base line, the curve monitoring the absorption at 1160 cm^{-1} shows an offset of $\sim 10\,\mathrm{mAU}$.

Time (s)	Glycerol (mL)	Xanthan Gum (g)
84	5.0	-
245	5.0	-
350	-	3.31
735	5.0	-
840	5.0	-
1050	-	3.80
1470	5.0	-
1680	5.0	-
2380	-	3.47
2590	5.0	-
2940	5.0	-
3220	-	3.96
3640	5.0	-
3850	5.0	-
4130	-	2.34

Table 3.5.: Spiking the laboratory vessel with glycerol and xanthan gum.

(a)   (b)
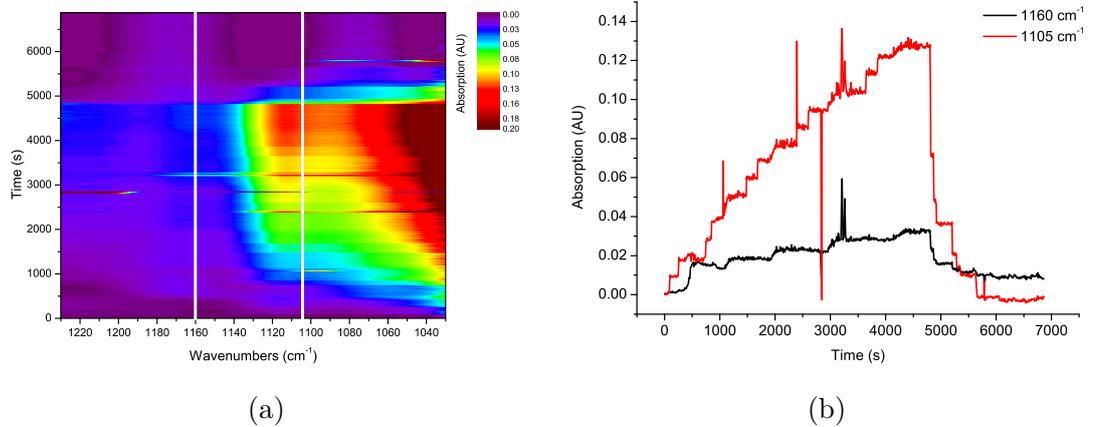
Figure 3.7.: Spiking the laboratory vessel with glycerol and xanthan gum and monitoring it in scan mode. (a): Absorption indicated as color-map, (b): step-wise increase of absorption at $1105\,\mathrm{cm^{-1}}$ and $1160\,\mathrm{cm^{-1}}$ (white lines in (a)).

3.1.5. Industrial Vessel with CIP-Equipment at the Vienna University of Technology

The first experiments performed at the industrial CIP plant included testing of different flow rates for cleaning the vessel, hence the process water was recirculated in the system. The installed spray ball was *Sani Midget*, the tracer substance glycerol and the CIP pumps were set to $2000\,\mathrm{kg\,h^{-1}}$ and $5000\,\mathrm{kg\,h^{-1}}$. Figure 3.8 shows the resulting curves, the PATOV-Sensor recorded the absorption at $1113\,\mathrm{cm^{-1}}$. In fig. 3.8a one can see that the signal increased the first time at $t \sim 80\,\mathrm{s}$, which was caused by activation of the gear pump. The CIP process pumps were started at the same time and the absorption increased $25\,\mathrm{s}$ later due to the removal of the tracer from

the walls of the vessel. Two smaller peaks can be identified at $t = 210\,\mathrm{s}$ and $300\,\mathrm{s}$. Moreover, the signal stabilized at $t \sim 350\,\mathrm{s}$ which indicated firstly, that the cleaning process was finished and secondly, that the glycerol was dissolved homogeneously by recirculation of the cleaning liquid. If the CIP pumps were set to $5000\,\mathrm{kg\,h^{-1}}$, the cleaning process finished much faster (fig. 3.8b). One can clearly see that the first peak at $t = 75\,\mathrm{s}$ is shorter, a second smaller peak occurs already $50\,\mathrm{s}$ later and the whole cleaning process was finished within $150\,\mathrm{s}$.

(a)   (b)
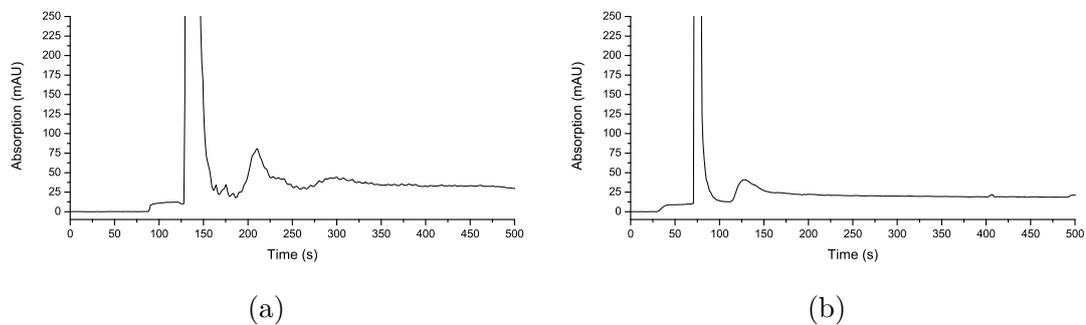
Figure 3.8.: Influence of different pump rates: (a): $2000\,\mathrm{kg\,h^{-1}}$, (b): $5000\,\mathrm{kg\,h^{-1}}$ (sprayball: *Sani Midget*, contaminant: glycerol).

The next two experiments used the spray ball *Rensekugler* and the CIP pumps were set to $2000\,\mathrm{kg\,h^{-1}}$. At first it was tested with glycerol and for the second run a mixture of glycerol and xanthan gum was prepared. The absorption curves, again recorded at $1113\,\mathrm{cm^{-1}}$, are shown in fig. 3.9. As it can be seen in fig. 3.9a, the *Rensekugler* caused more and sharper peaks during the cleaning process, but the critical parameter, namely the time it takes until the vessel was cleaned, was almost the same. Adding xanthan gum to the glycerol didn't have any influence on the cleaning efficiency of the spray ball (fig. 3.9b). The short decrease of absorption at

$t = 600\,\mathrm{s}$ was caused by injecting ethanol into the flow cell and switching back to the process stream.
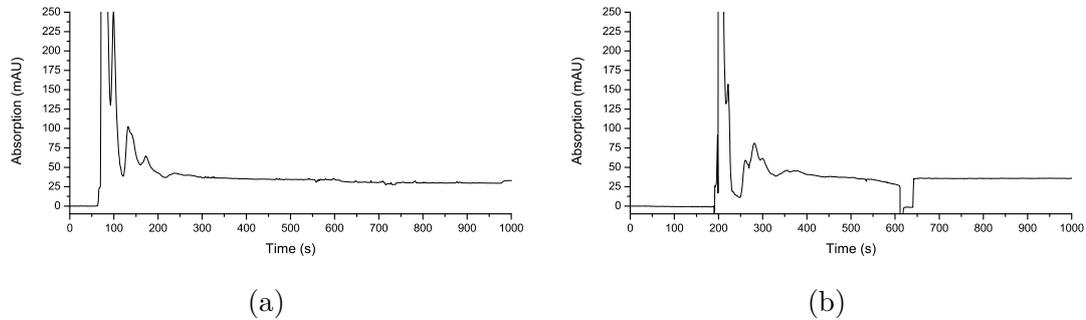
Figure 3.9.: Cleaning process with different contaminants: (a): glycerol, (b): glycerol and xanthan gum (pump rate: $2000\,\mathrm{kg\,h^{-1}}$, spray ball: *Rensekugler*).

The plots shown in fig. 3.10 are the results of monitoring the CIP process in scan mode. Like in fig. 3.7a, the absorption is indicated by the color and every $7\,\mathrm{s}$ a new spectrum was recorded. Similar to the single-wavelength-experiments, a strong absorption peak at the beginning of the cleaning (fig. 3.10a, $t = 490\,\mathrm{s}$; fig. 3.10b, $t = 100\,\mathrm{s}$) was followed by multiple smaller ones. Moreover, one can see that in the experiment, which involved glycerol as the only tracer substance, the walls of the vessel were cleaned after $\sim 100\,\mathrm{s}$. In contrast, the duration until the absorption was stable again was $\sim 300\,\mathrm{s}$ when using a mixture of glycerol and xanthan gum. Comparing this result to the previous ones where the absorption was recorded at a single wavelength, one can see that the repeatability is limited and only trends can be estimated.

While the previously discussed experiments were performed by recirculating the cleaning liquid, the following two were done in *rinse* mode, redirecting the process

(a)   (b)
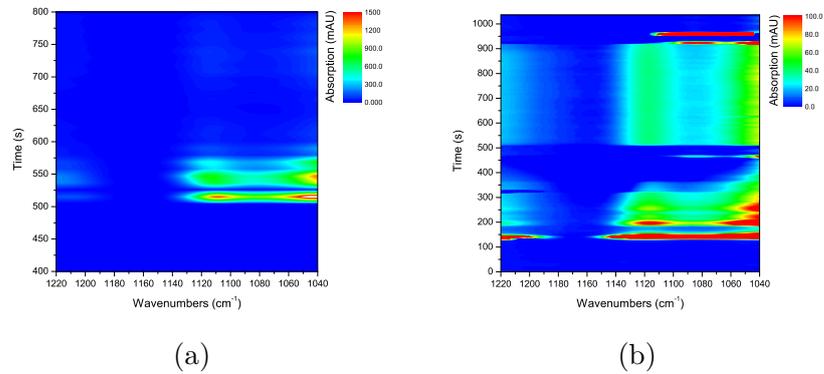
Figure 3.10.: Monitoring the cleaning process of the CIP vessel in scan mode. (a): glycerol, (b): glycerol and xanthan gum.

water from the output of the vessel to the drain. The result of using glycerol as tracer substance is shown in fig. 3.11a whereas the PATOV sensor was set to $1113\,\mathrm{cm}^{-1}$. Figure 3.11b, in contrast, was recorded at $1080\,\mathrm{cm}^{-1}$ as only xanthan gum was distributed at the walls of the vessel. Again, the signal stabilized $\sim 150\,\mathrm{s}$ after the CIP pumps were started. In comparison to the *cycle* experiments, the absorption went back to $0\,\mathrm{mAU}$ for glycerol and to $\sim 3\,\mathrm{mAU}$ for xanthan gum.

(a)   (b)
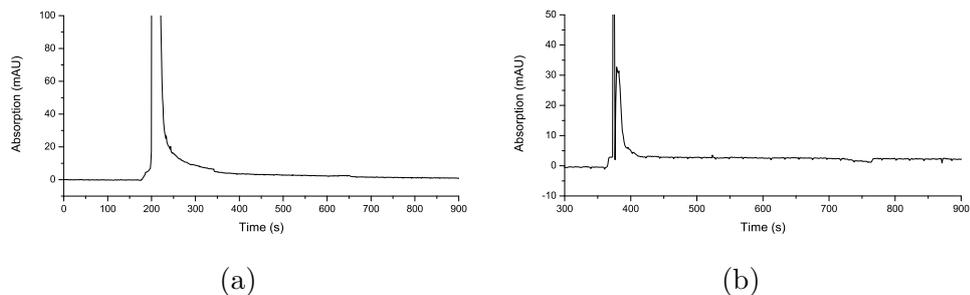
Figure 3.11.: Cleaning process while redirecting the process water to the drain (*rinse* mode): (a): glycerol, (b): xanthan gum.

3.1.6. Industrial Vessel with CIP-Equipment at CMC Biologics

The following results were gained during a measurement campaign at the cooperation partner CMC Biologics. Due to the limited time, only a small number of experiments could be executed.

Similar to the experiments with the industrial vessel at the Vienna University of Technology, the surface of the vessel was coated with glycerol (100 mL) and then cleaned by the CIP system. Moreover, the gear pump was located next to the outlet of the vessel and the cleaning progress was monitored with the PATOV sensor at $1113\,\mathrm{cm}^{-1}$. The most promising results are shown in fig. 3.12.
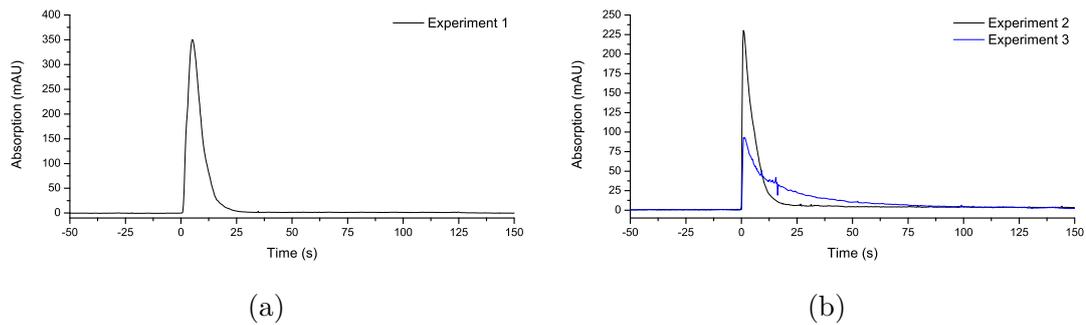
Figure 3.12.: Three cleaning processes at CMC Biologics: (a): spray ball: *HAKE small*, pump rate: $490\,\mathrm{kg\,h}^{-1}$; (b): two experiments with identical parameters (spray ball: *Hake X1-1*, pump rate: $1370\,\mathrm{kg\,h}^{-1}$).

The limited number of successful cleaning experiments allow only vague conclusions. At first glance, it seems that neither the pump rate nor the spray ball have a significant influence of the cleaning time (experiment 1 vs. experiment 2). After repeating

experiment 2 with the same parameters (experiment 3), one has to reject that assumption as the cleaning process takes approximately two times longer. Nevertheless, it has to be noted that the integral of the absorption curves fit to 94 %.

3.2. Ring-Cavity Surface Emitting Lasers

Three wafers with each 96 ring-CSELs were processed within this work. A detailed overview of the grating periods and their expected emission wavelengths is given in appendix B.4.

The characterization of the manufactured QCLs showed that most of the lasers emit single-mode only at low currents (typically up to $1.3\times J_{th}$) and that multi-mode emission dominated over the whole gain region ($\sim 50\,\mathrm{cm}^{-1}$) at higher currents. As single-mode operation and high optical power are crucial for precise spectroscopy, only three lasers with acceptable emission behavior are depicted in fig. 3.13.

Taking a closer look at the lasers shown in fig. 3.13a and fig. 3.13b, one can clearly see that the desired emission wavelength is available over the whole current range and the multi-mode behavior begins at $\sim 1.1\,\mathrm{A}$. In contrast, the third ring-CSEL (fig. 3.13c) emits single-mode at an unwanted wavelength ($1490\,\mathrm{cm}^{-1}$) until $\sim 1.3\,\mathrm{A}$. When the current is further increased, the laser begins emitting at the designed wavelength ($1532\,\mathrm{cm}^{-1}$) and the lasing mode at $1490\,\mathrm{cm}^{-1}$ gets significantly damped.

However, the optical power and spectral properties of the manufactured ring-CSELs are improvable. One possible approach to achieve single-mode devices with sufficient power could be increasing the etching depth of the grating. Other steps for optimizing the emission behavior of the lasers could be testing different duty cycles of the grating as well as manufacturing devices with different ridge widths.
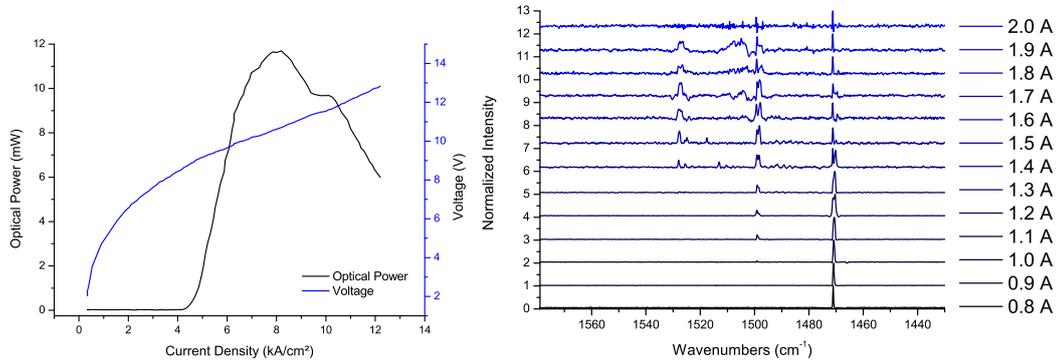
(a) Designed wavelength: $1472\,\mathrm{cm}^{-1}$, 580 grating slits
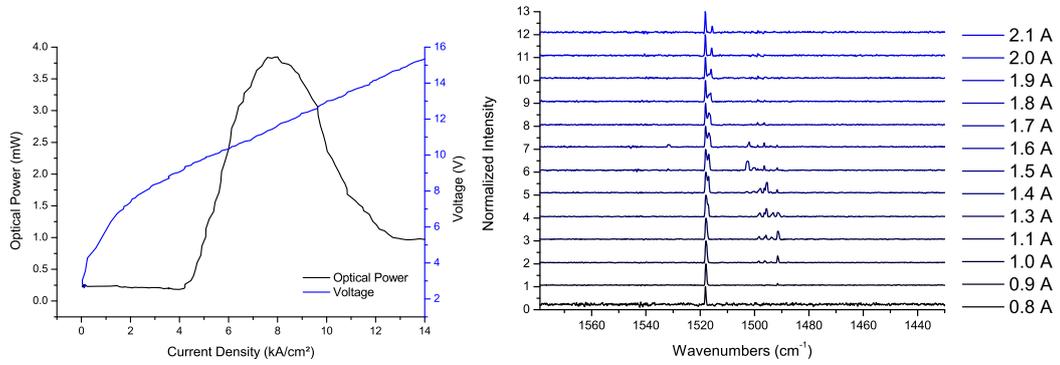
(b) Designed wavelength: $1517\,\mathrm{cm}^{-1}$, 600 grating slits
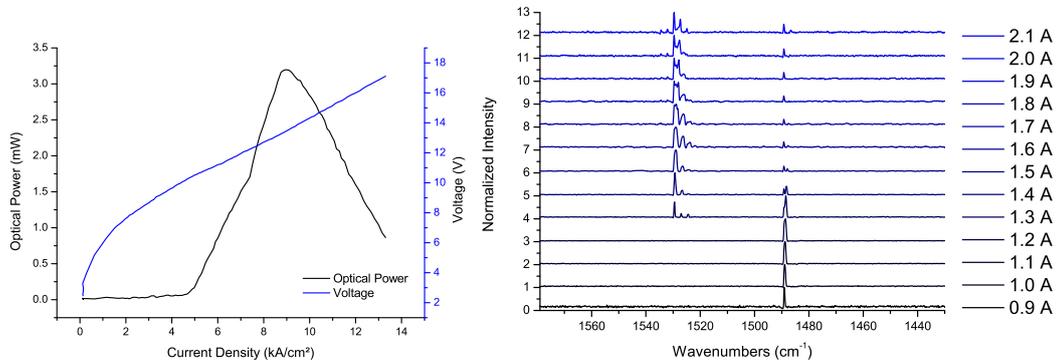
(c) Designed wavelength: $1532\,\mathrm{cm}^{-1}$, 608 grating slits

Figure 3.13.: LIV curves and spectra at different currents of three ring-CSELs.

Chapter 4.

Conclusion and Outlook

The experiments performed within this thesis show that infrared sensors based on quantum cascade lasers are an emerging and powerful tool in process analytical chemistry. The benefits of the developed prototype compared to traditional TOC analyzers are the much shorter time delay, continuous operation during a cleaning process and chemical information can be gained as well if the EC-QCL is operated in scanning mode.

The figures of merit of the PATOV-Sensor were evaluated in different ways. Firstly, spectra of two tracer substances, namely glycerol and xanthan gum, were recorded at different concentrations. Secondly, calibration curves at $1113\,\mathrm{cm^{-1}}$ were calculated whereas the LODs are 88.5 ppm for glycerol and 122.6 ppm for xanthan gum. Thirdly, the optimum settings for the sensor interface were identified and the resulting time delay was measured to be $\sim 6\,\mathrm{s}$.

After characterizing the sensor parameters, the device was tested together with a laboratory vessel, an industrial scale plant at the Vienna University of Technology and at the project partner CMC Biologics. While the first one was only suited for recirculation experiments, the second one was identical to industrial plants and allowed therefore both, recirculation and rinse tests. Hereby, the effect of different CIP pump speeds and sprayballs were shown as well. Finally, experiments at the project partner CMC Biologics showed that cleaning a vessel is always slightly different and that monitoring the cleaning process could shorten the down time of industrial plants (appendix A, [70]).

However, the PATOV-Sensor has still potential for improvements. The major limiting part within the setup is the EC-QCL, due to its wavelength selection technique. The synchronization of the mechanical grating influences the spectral precision and stability. The origin of this limitation is described elsewhere in detail [71, 72] and can be improved by additional signal processing [73]. In addition, newer EC-QCLs already allow a spectral acquisition rate of $20\,\mathrm{Hz}$ over $1145\text{--}1265\,\mathrm{cm}^{-1}$ [74]. Another improvement could be done by replacing the EC-QCL by a DFB-QCL- or ring-CSEL-array. The benefit is that mechanical parts can be completely avoided and the wavelength selection is done by pulsing different lasers with different DFB-grating-periods within one wafer [75, 76].

To be more flexible concerning the contaminations produced in the fermentation process, the spectral range should be extended as well. Therefore, the processing of ring-CSEL in the range of the amide-II absorption band was shown in this thesis. However, its integration into the optical setup of the PATOV sensor will be part of future work.

Beside optimizing the light source, one could improve the flow cell design as well. For example, the CaF_2 windows could be replaced with polyethylene (PE)- or diamond-like carbon (DLC)-coated ones, making them more robust against cleaning agents such as acids. Moreover, a microfluidic integration as suggested in [65] is possible as well. Herein, a miniature flow cell would be realized directly on a QCL/QCD chip. Another approach is shown in [77, 78] whereas waveguides are responsible for the sample interaction.

Although the PATOV-Sensor shows a lot of potential in improving its properties in different ways, it has to be noted that it is already a powerful tool in CIP processes. The successful implementation of the prototype at the project partner CMC Biologics (Copenhagen) could be the base for new CIP designs and could optimize production processes as well.

Appendix A.

Scientific Paper about PATOV

Online Monitoring of TOC Contaminations in Clean-in-Place Processes for Optimized Process Control, Increased Process Efficiency and Quality

Tanja Siegmann-Hegerfeld, Andreas Genner, Markus Brandstetter, Martin Miltner, Bernhard Lendl, Michael Harasek

Online Monitoring of TOC Contaminations in Clean-in-Place Processes for Optimized Process Control, Increased Process Efficiency and Quality

Tanja Siegmann-Hegerfeld[a], Andreas Genner[b], Markus Brandstetter[b], Martin Miltner[a], Bernhard Lendl[b], Michael Harasek[a],*

[a]Institute of Chemical Engineering, Vienna University of Technology, Getreidemarkt 9/166, A-1060 Vienna
[b]Institute of Chemical Technologies and Analytics, Vienna University of Technology, Getreidemarkt 9/164, A-1060 Vienna
michael.harasek@tuwien.ac.at

A Process Analytical Technology (PAT) compliant unit (acronym PATOV) was designed for online monitoring of Clean-in-Place (CIP) processes used in the pharmaceutical and food industry. The PATOV unit tends to significantly optimize CIP processes by online monitoring Total Organic Carbon (TOC) equivalent contaminations in the CIP off-stream to increase the efficiency and the quality of the cleaning process. The data will be used for an online control of the process to ensure optimal cleaning in minimized time. This will certainly allow for extensive savings of energy, water, and cleaning agents. Commercially available TOC analyzers qualified for the purpose require several minutes to provide a reliable TOC result. By implementing a mid-IR laser absorption technology, more precise a sensor based on an External Cavity-Quantum Cascade Laser (EC-QCL), the necessary information can be gained within seconds. An experimental CIP pilot plant was installed to reproduce CIP procedures by cleaning a vessel of a typical size used in pharmaceutical production processes. A continuous sample flow is gathered from the CIP off-stream and fed into the PATOV unit which is placed close to the CIP pilot plant. The contamination of the CIP process water can be measured with a time resolution down to one second. The retention time of contaminations from the CIP pilot plant to the PATOV unit was minimized to <10 s by the design of an optimized sampling system. Currently, the TOC can be detected within the short timelines mentioned for single contaminants down to a concentration of e.g. 20 ppm for glycerol. Provided that the detection of lower concentrations and the calibration for other model contaminants, such as xanthan and proteins can be achieved, the PATOV unit has a high potential to improve the efficiency and the quality of CIP processes in the pharmaceutical and food industry.

1. Introduction

The cleaning of production equipment in pharmaceutical and food industry is a crucial part of the production process. While the invention and further development of automated CIP systems decades ago substantially increased the reliability and efficiency of the cleaning processes compared to manually cleaning by process operators, still a high potential for improvement of the cleaning processes remains. CIP equipments provide Water for Injection (WFI) along with cleaning agents at predetermined temperatures and pressures for realization of preconfigured cleaning cycles. To guarantee high level regulations demanded by the Food and Drug Administration (FDA) and other regulatory institutions (US FDA - CDER, 2005), the cleaning cycles usually last considerably longer than necessary. Typically, laboratory testing of a sample taken from the final rinse verifies if the requirements are fulfilled and the production process can resume. Apparently, this approach leads to waste of water, cleaning agents and energy and additional to long periods of process downtime.

Today, an established approach to verify cleaning processes is the quantification of the TOC in CIP off-stream samples. An overview on cleaning validation is e.g. given by Lakshmana (2010), savings strategies for cleaning fluids have been investigated e.g. by Dif et al. (2012). Analyzing a sample for TOC is typically based on entirely oxidizing the sample. Thus every contained carbon atom reacts to CO_2 which can be quantified using dispersive near-infrared techniques. While by now several online TOC analyzers are commercially available, as far as we know, up to now none of them is suitable for covering the whole cleaning process regarding a real time validation from very high (>10^4 ppm) down to very low TOC (<1 ppm) contaminations. Commercially available online TOC analyzers to be considered for this task typically provide results with a frequency of several minutes. Even if the actual measurement time might be shorter, cleaning procedures or sample preparation extend the time before the analyzer can measure the next sample.

To significantly optimize CIP processes by introducing an online, real time cleaning validation system a PAT compliant unit (acronym PATOV) was designed for online monitoring. The PATOV unit intends to ensure optimal cleaning, while simultaneously controlling cleaning time and cleaning agents used and to provide additional analytical information. The optimized process control has a high potential to significantly increase process efficiency and quality and therefore reduce cleaning costs and process downtime.

The PATOV unit is based on a mid-infrared (mid-IR) laser absorption technology. The application of mid-IR spectroscopy to monitor the cleaning process is a promising alternative to the use of commercially available TOC analyzers. The mid-IR spectral region includes electromagnetic radiation with wavelengths between ~3 μm and ~20 μm. In this spectral region the fundamental vibrational states of molecules can be found, i.e. that molecules irradiated with mid-IR light will show absorption of specific wavelengths. According to the Beer-Lambert law, the concentration of an analyte can be determined by the amount of the absorbed light. The Beer-Lambert law is defined as

$$A = -\log I / I_0 = \alpha \cdot c \cdot d \tag{1}$$

where I is the intensity spectrum of the sample [a.u.], I_0 the intensity spectrum of the background or solvent [a.u.], α the molar absorption coefficient [L mol^{-1} m^{-1}], *c* the sample concentration [mol L^{-1}] and *d* the interaction length (= optical pathlength in the sample) [m]. Mid-IR absorption spectroscopy is molecular specific, direct and reagent-free. It offers online capability and quasi-continuous measurements with time resolutions down to <1 s. It is therefore a promising technique for application to process monitoring in CIP environment.

2. Experimental CIP pilot plant

To optimize process equipment and for testing of the PATOV unit, a base case CIP system was configured and installed. The base case was defined with regard to real pharmaceutical CIP systems, though the design was limited to necessary procedures and equipment sufficient for the testing purpose. The pilot plant enables to reproduce CIP procedures by cleaning a vessel of a typical size used in pharmaceutical production processes. A picture of the experimental CIP pilot plant is shown in Figure 1. It consists of a water storage tank, a heat exchanger, pumps for cycling the water and the connecting pipes. The vessel is located in the center of the pilot plant. A spraying device installed in the lid of the vessel delivers the cleaning fluid to the walls.

Figure 1: Experimental CIP pilot plant.

Table 1: CIP steps

Step	Notation	Liquid	Temperature	Operation
1	1st rinse	WFI	ambient	once through
2	1st wash	WFI, NaOH, 2%	70 °C	recycle 15 - 60 min
3	2nd rinse	WFI	ambient	once through
4	2nd wash	WFI, HNO$_3$, 2%	ambient	once through
5	Final rinse	WFI	ambient	once through

To avoid build-up fluid in the vessel, a self-priming pump is mounted on the CIP system. It is used to pump the fluid out of the vessel, either back to the water storage tank for recirculation or directly to the drain. The experimental CIP pilot plant covers the major process challenges existing in real pharmaceutical CIP systems. The pilot plant is equipped with additional instruments and signals for experimental investigations. The gained supplemental data are used for optimization of the CIP system. Three sampling points are implemented to verify the optimal location for the PATOV unit, which have been identified by CFD simulations. To retrieve a gas free sample for the PATOV unit an additional separator unit was developed and installed. Finally, successive CIP steps (listed in Table 1) have been defined to represent the model process.

3. PATOV analytical unit

The PATOV unit with the implemented IR equipment is placed close to the CIP pilot plant. The PATOV unit consists of several components which are assembled in a custom built frame made out of aluminum profiles and aluminum boards with protective covers of acrylic glass (not shown). A scheme with the major parts and connections is shown in Figure 2.
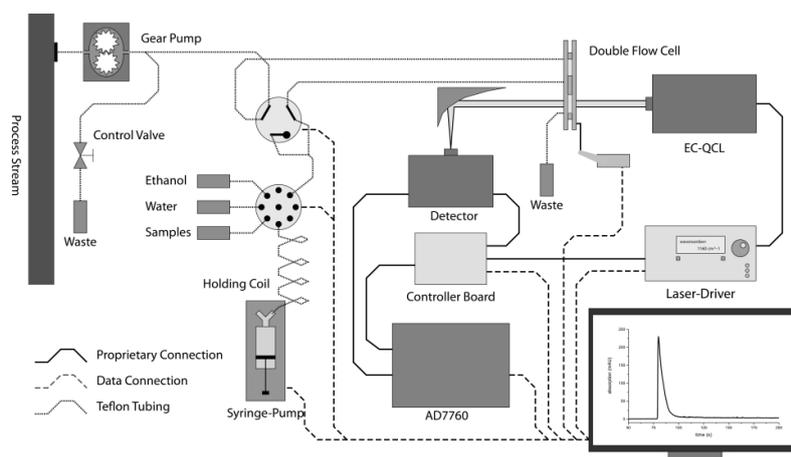

Figure 2: Scheme of the PATOV analytical unit

The core element of the PATOV unit is the mid-IR absorption set-up consisting of the mid-IR laser light source, a transmission flow cell where the sample is placed into the optical path, and a thermoelectrically cooled mercury cadmium telluride (MCT) infrared detector. A novel broadly tunable QCL (Daylight Solutions Inc., USA) is used as light source. Compared to standard Fourier Transform IR (FTIR) spectrometers, the light intensity is much higher (more than four magnitudes higher than for glow bars) and the emitted wavelength can be controlled electronically, resulting in a device without an interferometer. The wavelength is set by an internal rotating grating that enables the laser to emit from 1,030 to 1,230 cm^{-1}. Tuning over the whole emission range and moving back to the start point takes ~4 s. The maximum spectral emission power density is approximately 350 mW. The transmission flow cell consists of two CaF$_2$ windows that are separated by a 160 µm layer of Polytetrafluoroethylene (PTFE) and an aluminum construction, holding the parts together. Due to the high intensity of the QCL, the optical path length is increased compared to conventional FTIR spectroscopy. The increased path length reduces the vulnerability to clogging which is an important factor in practical field application. As the laser beam is

981

~3 mm in diameter, an off-axis parabolic mirror is used to focus the light onto the detector element (element size ~1x1 mm). Conventional detectors in mid-IR spectroscopy require liquid nitrogen cooling which makes them unsuitable for applications outside the lab. To circumvent that, a MCT-detector with an implemented Peltier cooling element is used. This cools the detector element down to -58 °C. Due to the MCT-technology, every single laser pulse (repetition rate: 100 kHz) can be resolved.

The interface between the PATOV unit and the CIP pilot plant is realized by a bypass system consisting of a gear pump, a T-connector and a control valve. The injection valve (6-port, VICI, Switzerland) offers the possibility to select between the process stream and the calibration channel with the cleaning agent or the calibration samples (Figure 2) to be directed to the transmission flow cell. Every analyte shows different extinction coefficients, depending on the used wavelength. In order to calculate the proper contaminant concentration those coefficients have to be determined. This is done by measuring samples with different concentrations of the analyte/contaminant and fitting an appropriate calibration curve. Hence, a calibration channel is used for injection of the background liquid (WFI) and for cleaning the transmission flow cell as well as for injection of off-line samples used for calibration of the prototype device.

The PATOV analytical unit offers two modes of operation – scan mode and single wavelength mode. In scan mode a full absorption spectrum of over 200 cm^{-1} (maximum tuning range of the currently used QCL) is recorded. The spectral information offers the possibility to not only measure the amount of contamination but to even discriminate between the type of contamination. The time resolution in scan mode is currently limited to 6 s (limited by the used QCL). In contrast to that the single wavelength mode increases the time resolution to values <1 s. However, it is only possible to measure at a single emission wavelength, i.e. there is no spectral information available.

4. Results

Two different CIP steps (see Table 1) have been investigated: rinses and recycles. In both configurations either a single contaminant or a mixture of two contaminants (glycerol, xanthan, soy peptone) has manually been placed into the reaction vessel. The results presented here are restricted to glycerol contaminations, ambient temperature and Water/WFI as cleaning fluid (no caustic). The CIP system was activated and the contaminated off-stream process water was measured on-line by the PATOV unit. In recycle mode the cleaning water was pumped in a closed cycle. In rinse mode the cleaning water was pumped once through to the drain. For reference measurements samples were manually taken at defined intervals. The TOC measurements were conducted afterwards off-line using a Shimadzu TOC-VCSH/CSN TOC Analyzer.

4.1 Calibration

Calibration was performed by measuring a number of predefined glycerol solutions with the PATOV analytical unit. Data were acquired in single wavelength mode and served as calibration for calculating the TOC level which corresponds to the measured absorption. To improve the calibration a second procedure was tested by using a vessel equipped with a stirrer. The water in the vessel was weighed and defined amounts of tracer substance were added in steps. A calibration curve was calculated by averaging ten data points, ten seconds after each spiking step. This procedure resulted in a higher linearity compared to the manual calibration procedure. The calibration data are given in Table 2.

Table 2: Calibration data

first calibration	second calibration
R^2 = 0.9993	R^2 = 0.99986
LOD_{TOC} ~ 90 ppm	LOD_{TOC} = 20.6 ppm

4.2 Laboratory experiments

Laboratory experiments were conducted using the experimental CIP pilot plant described in Section 2. An example of an on-line measurement performed in scan mode is shown in Figure 4(a). The reaction vessel was contaminated with approx. 1,000 g glycerol (operating conditions: flowrate: 2,000 kg/h, temperature ~20 °C, vessel volume 320 L, spray ball Sani Midget). The start of the cleaning process is indicated by the dashed arrow. The CIP system was used in recycle mode. Therefore, the contamination peaks reappear several times before further cycling has no impact anymore since the contamination is evenly distributed in the process water. The dotted arrow indicates a cleaning step of the flow cell. After the cleaning step, the glycerol contamination remains constant. Clearly the scan mode offers extensive spectral information of the contamination, yet the time resolution is significantly decreased compared to single wavelength mode.
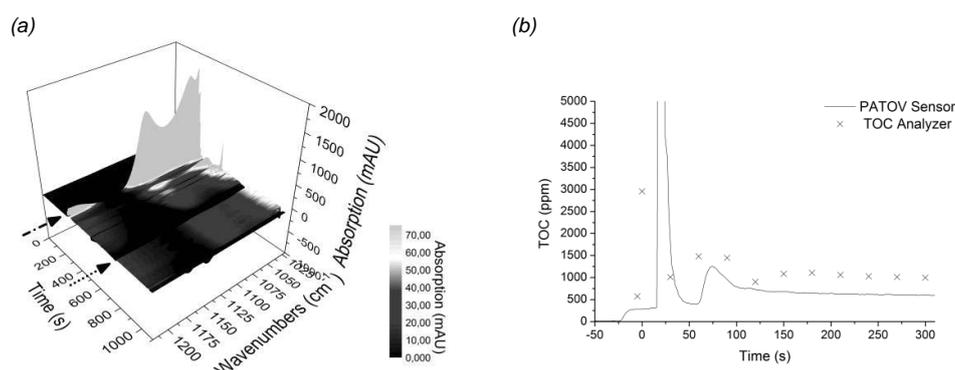
(a)

(b)

Figure 4: Cleaning cycle with glycerol as contaminant measured in scan mode (a) and measured in single wavelength mode (b). Measurement results for TOC off-line samples are included by symbols

In Figure 4(b) an example of a glycerol recycle performed in single wavelength mode is shown (operating conditions: contamination approx. 1,000 g glycerol, flowrate 2000 kg/h, temperature ~20 °C, vessel volume 320 L, spray ball Sani Midget). The absorption measured by the PATOV analytical unit was converted to a TOC equivalent using the calibration data given in Section 4.1 (first calibration). The TOC equivalent is shown as a function of time. Even though the cleaning effect depends on various parameters (e.g. flow rate, spray ball, contamination), all measured TOC curves exhibit basically similar progressions like the example shown in Figure 4(b). A first peak appears only a couple of seconds after starting the CIP process as the distance between the contaminated vessel and the sampling unit is very short. After the process water has passed one cycle a second peak is visible, which indicates that the cleaning is still productive. Finally the TOC approaches an asymptotic behavior indicating that further operation will not be worthwhile. The signal gained by the PATOV unit provides valuable on-line process information. Samples for TOC off-line measurements have been taken every 30 s during the cleaning cycle. The measurement results are included by symbols. Evidently, the results show large quantitative deviations, while qualitative agreement is obtained regarding the progression.

4.3 Field operational tests

Field operational tests were conducted at a Biopharmaceutical Contract Manufacturing company (project partner CMC Biologics A/S in Copenhagen, Denmark) using a simplified version of the experimental CIP pilot plant (see Section 2). The most important differences were the use of a slightly smaller vessel (Sartorius BBI Biostat D), single pass flow of cleaning liquids and that the separation unit was not included. Only rinse steps have been tested due to operational restrictions. The experiments were performed by initially filling the water storage tank with high purity water and heating the water up to approximately 20 °C. Afterwards the vessel was contaminated with 100 g pure glycerol using a syringe. The cleaning process was started by pumping the high purity water into the spray ball and cleaning subsequently the vessel. The gear pump, which transported the liquid from the bottom of the vessel to the PATOV unit, was started with a delay of approximately 3 s to make sure that the sample point is filled with water. The signal of the PATOV unit was recorded with a data rate of approximately 3 data points per second.

Some promising results have been obtained. One example is shown in Figure 5(a) (operating conditions: flowrate: 490 kg/h, temperature ~20 °C, vessel volume 150 L, spray ball small HAKE). The continuous lines represent the data of the PATOV unit and the symbols are the results off-line sample measurements. Again the off-line measurements show significant deviations, but a qualitative agreement regarding the progression. Certainly various errors have to be considered with the comparison, in particular differing sampling volumes and sampling positions. The PATOV unit works with a continuous pump flow and small dead volume. Each offline sample contained approximately 50 mL of cleaning liquid and it took 2 to 5 s to take each sample. Further examples are presented in Figure 5(b) (operating conditions: flowrate: 1,370 kg/h, temperature ~20 °C, vessel volume 150 L, spray ball big HAKE type X1-1). Data of the PATOV unit are shown for two experiments conducted for identical parameters (flow rate, spray ball, temperature, type and amount of contamination, etc.). The curves show a significant difference, which can be expected due to diverging cleaning effects from the different start contaminations at the vessel surface. In fact the line integral matches in the order of about 94 %.

983

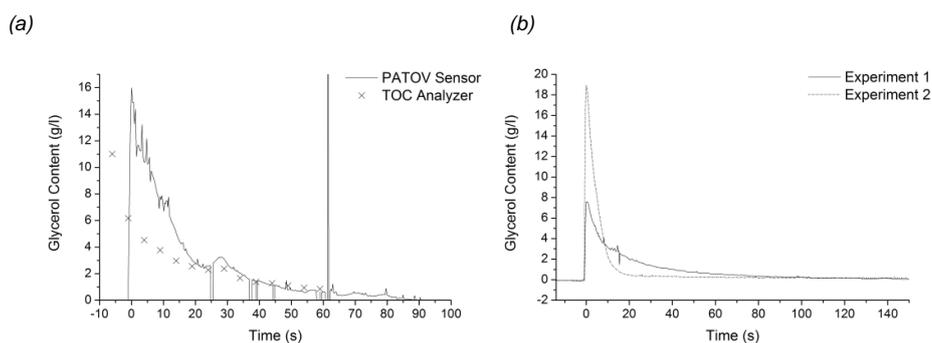(a)   (b)

Figure 5: Rinse tests with glycerol as contaminant measured in single wavelength mode (a, b). The measurement results for TOC off-line samples are included by symbols (a).

5. Summary and conclusions

Based on mid-IR absorption the new developed PATOV unit offers quasi-continuous measurements with time resolutions down to one second. Bearing in mind that the time delay caused by the sampling system is in the order of 10 s, the PATOV unit enables online monitoring of CIP processes. The PATOV unit was successfully applied to experimental CIP process equipment. Calibration for glycerol was conducted with high linearity down to a detection limit of 20 ppm. First laboratory experiments and field operational tests show promising results. Valuable process information was gathered which could be used to significantly optimize the cleaning procedures resulting in increased process efficiency and quality. It has to be emphasized that the sampling position must be well chosen and short connection lines to the PATOV unit have to be established. Also, experimental data with regard to IR-QCL / TOC comparison have to be considered as preliminary. TOC measurement of off-line samples show large quantitative deviations - partly due to a difficult sampling situation at the plant site, therefore validation of the on-line data will be a very important target for future investigations. Extension of the analytical device for application to proteins is currently being processed by manufacturing a QCL light source for the protein spectral region. Improving the detection of lower concentrations and calibrating for other model contaminants and real-world contaminations will be objectives for further investigations. Future applications of the PATOV unit may also involve CIP of food processing plants.

References

Dif M., Blel W., Sire O., 2012, New physico-chemical regeneration process of CIP solutions, Chemical Engineering Transactions, 29, 829-834
Lakshmana Prabu S., Suriyaprakash T.N.K., 2010, Cleaning Validation and its importance in Pharmaceutical Industry, Pharma Times, 42/07, 21-25
US FDA - CDER, 2005, Questions and Answers on Current Good Manufacturing Practices, Good Guidance Practices, Level 2 Guidance – Equipment <www.fda.gov/Drugs/GuidanceCompliance RegulatoryInformation/Guidances/ucm124777.htm#TOC> accessed 22.03.2013

984

Appendix B.

Ring-cavity Surface Emitting Lasers

B.1. Processing Parameters

B.1.1. 2nd Order Grating

rem. oxides	20% KOH, 1 min	2 min rinse		
e-line	AR-P679.04	35 s @ 2000 rpm		
		baking	5 min	170 °C
		exposure	dose factor 0.8	
		developing	AR600-56	40–60 s
		stopper	IPA	
evap. metal	Ti	150 Å		
	Au	500 Å		
	Ni	1800 Å		
lift-off	NEP	2 h @ 150 °C		
		ultrasonic bath	2 min @ 10%	
rie	1.6 µm	etch rate	100 nm min^{-1}	Si-carrier
	p_{work}	2 mtorr	p_{strike}	40 mtorr
	SiCl$_4$	5 sccm	Ar	40 sccm
	RF	200 W	T	250 °C

B.1.2. Hard Mask

pecvd - Si_3N_4	1000 nm	rate:		
		$10\,nm\,min^{-1}$		
	p_{base}	0.66 torr	p_{work}	1 torr
	SiH_4	700 sccm	NH_3	18 sccm
	RF	11 W	T	300 °C
lithography	AZ5214 (1:0)	35 s @ 4000 rpm		
		baking	1 min	100 °C
		exposure rims	50 s	
		developing	AZ351B (1:4)	40 s
		exposure rings	5 s	
		developing	AZ351B (1:4)	8 s
rie	1000 nm	etch rate	$100\,nm\,min^{-1}$	quartz-carrier
	p_{work}	15 mtorr	p_{strike}	40 mtorr
	SF_6	40 sccm		
	RF	60 W	T	30 °C
pl. oxidation	10 min @ 300 W			
	ultrasonic bath	30 s @ 10%	acetone, IPA	

B.1.3. Waveguide

rie	7 µm	etch rate	$100\,nm\,min^{-1}$	Si-carrier
	p_{work}	2 mtorr	p_{strike}	40 mtorr
	$SiCl_4$	5 sccm	Ar	40 sccm
	RF	200 W	T	250 °C
rie	4 min			quartz-carrier
	p_{work}	15 mtorr	p_{strike}	40 mtorr
	SF_6	40 sccm		
	RF	60 W	T	30 °C
rie	4 min			quartz-carrier
	p_{work}	50 mtorr	p_{strike}	40 mtorr
	SF_6	40 sccm		
	RF	50 W	T	30 °C

B.1.4. Insulation

pecvd - Si_3N_4	300 nm	rate:		
		$10\,\text{nm}\,\text{min}^{-1}$		
	p_{base}	0.66 torr	p_{work}	1 torr
	SiH_4	700 sccm	NH_3	18 sccm
	RF	11 W	T	300 °C
lithography	maP1275	35 s @ 9000 rpm		
		baking	5 min	100 °C
		exposure rims	50 s	
		developing	maD331	60 s
		exposure rings	9 s	
		developing	maD331	40 s
rie	300 nm	etch rate	$100\,\text{nm}\,\text{min}^{-1}$	quartz-carrier
	p_{work}	15 mtorr	p_{strike}	40 mtorr
	SF_6	40 sccm		
	RF	60 W	T	30 °C
rie	3 min			quartz-carrier
	p_{work}	50 mtorr	p_{strike}	40 mtorr
	SF_6	40 sccm		
	RF	50 W	T	30 °C
pl. oxidation	10 min @ 300 W			

B.1.5. Top Contact

lithography	hmds	35 s @ 4000 rpm		
		baking	30 s	100 °C
	maP1275	35 s @ 9000 rpm		
		baking	5 min	100 °C
		exposure rims	50 s	
		developing	maD331	60 s
		exposure rings	9 s	
		developing	maD331	40 s
pl. oxidation	1 min @ 300 W			
sputtern	p_{base}	2×10^{-5} mbar	p_{work}	8×10^{-3} mbar
	Ti	4x30 s @ 25 W		
	Au	15x40 s @ 25 W		
lift-off	acetone	1 h @ 60 °C		

B.2. Top Down Processing Scheme

2nd Order Grating

Etching

Spin Coating

Exposure (E-Line)

Developing

Ti, Au Deposition

Lift Off

RIE Etching

Hard Mask

Si$_3$N$_4$ Deposition

Spin Coating

Exposure (Litho)

Developing

RIE Etching

Plasma Oxidation

Waveguide

RIE Etching

RIE Etching

Insulation

Si$_3$N$_4$ Deposition

Spin Coating

Exposure (Litho)

Developing

RIE Etching

Plasma Oxidation

Top Contact

Spin Coating

Exposure (Litho)

Developing

Sputtern

Lift Off

B.3. H861 Growth Sheet

Layer (Substrate to Surface)	x (%)	Thickness (nm)	Doping (Si)	Description
InP n-		-	2e17	Substrate
Si:$In_x Ga_{1-x}As$	53	2.5	1e17	
Si:$In_x Al_{1-x}As$	52	2.5	1e17	
Si:$In_x Ga_{1-x}As$	53	3.0	1e17	
$In_x Al_{1-x}As$	52	2.0	-	
$In_x Ga_{1-x}As$	53	3.5	-	
$In_x Al_{1-x}As$	52	1.5	-	
$In_x Ga_{1-x}As$	53	4.0	-	
$In_x Al_{1-x}As$	52	1.0	-	
$In_x Ga_{1-x}As$	53	4.5	-	
$In_x Al_{1-x}As$	52	0.5	-	
Si:$In_x Ga_{1-x}As$	53	500	5e16	Spacer
Loop 35				
$In_x Ga_{1-x}As$	53	3.8	-	Injection barrier
$In_x Al_{1-x}As$	52	2.9	-	
$In_x Ga_{1-x}As$	53	4.7	-	
$In_x Al_{1-x}As$	52	2.7	-	
$In_x Ga_{1-x}As$	53	5.9	-	
$In_x Al_{1-x}As$	52	1.7	-	
$In_x Ga_{1-x}As$	53	1.8	-	
$In_x Al_{1-x}As$	52	4.5	-	
$In_x Ga_{1-x}As$	53	2.4	-	
$In_x Al_{1-x}As$	52	2.7	-	
$In_x Ga_{1-x}As$	53	2.5	-	
$In_x Al_{1-x}As$	52	2.3	-	
$In_x Ga_{1-x}As$	53	2.6	-	
$In_x Al_{1-x}As$	52	2.2	-	
$In_x Ga_{1-x}As$	53	2.7	-	
$In_x Al_{1-x}As$	52	3.4	-	
Si:$In_x Ga_{1-x}As$	53	2.9	2.1e17	
Si:$In_x Al_{1-x}As$	52	3.2	2.1e17	
Si:$In_x Ga_{1-x}As$	53	3.2	2.1e17	
$In_x Al_{1-x}As$	52	3.1	-	
Endloop				

Layer (Substrate to Surface)	x (%)	Thickness (nm)	Doping (Si)	Description
Si:In$_x$Ga$_{1-x}$As	53	300	5e16	Spacer
Si:In$_x$Al$_{1-x}$As	52	0.8	1e17	
Si:In$_x$Ga$_{1-x}$As	53	4.2	1e17	
Si:In$_x$Al$_{1-x}$As	52	1.6	1e17	
Si:In$_x$Ga$_{1-x}$As	53	3.4	1e17	
Si:In$_x$Al$_{1-x}$As	52	2.5	1e17	
Si:In$_x$Ga$_{1-x}$As	53	2.5	1e17	
Si:In$_x$Al$_{1-x}$As	52	3.4	1e17	
Si:In$_x$Ga$_{1-x}$As	53	1.6	1e17	
Si:In$_x$Al$_{1-x}$As	52	4.2	1e17	
Si:In$_x$Ga$_{1-x}$As	53	0.8	1e17	
Si:In$_x$Al$_{1-x}$As	52	1500	1e17	Upper cladding
Si:In$_x$Al$_{1-x}$As	52	800	2e17	Upper cladding
Si:In$_x$Ga$_{1-x}$As	53	0.8	2e17	
Si:In$_x$Al$_{1-x}$As	52	4.2	2e17	
Si:In$_x$Ga$_{1-x}$As	53	1.6	2e17	
Si:In$_x$Al$_{1-x}$As	52	3.4	2e17	
Si:In$_x$Ga$_{1-x}$As	53	2.5	2e17	
Si:In$_x$Al$_{1-x}$As	52	2.5	2e17	
Si:In$_x$Ga$_{1-x}$As	53	3.4	2e17	
Si:In$_x$Al$_{1-x}$As	52	1.6	2e17	
Si:In$_x$Ga$_{1-x}$As	53	4.2	2e17	
Si:In$_x$Al$_{1-x}$As	52	0.8	2e17	
Loop 14				
Si:In$_x$Ga$_{1-x}$As	53	25	2e18	Contact layers
δ Doping			6e18	
Endloop				
Si:In$_x$Ga$_{1-x}$As	53	10	max.	Capping layer

B.4. Grating Periods of Processed ring-CSELs

No. of Grating Slits	Grating Period Λ (μm)	Expected Wavelength 293 K, $n_{eff} = 3.225$, (cm^{-1})
544	2.252	1377
552	2.220	1397
560	2.188	1417
568	2.157	1437
576	2.127	1458
580	2.112	1468
584	2.098	1478
588	2.084	1488
592	2.070	1498
596	2.056	1508
600	2.042	1518
604	2.029	1529
608	2.015	1539
612	2.002	1549
620	1.976	1569
624	1.963	1579
628	1.951	1589
632	1.939	1599

Bibliography

[1] D. A. Seiberling. "Introduction and Historical Development". In: *Clean-In-Place for Biopharmaceutical Processes*. Ed. by D. A. Seiberling. Volume 173. Informa Healthcare, 2008. Chap. 1, pp. 1–20. ISBN: 978-0-8493-4069-7.

[2] C. Lankford. "Cleaning Validation Strategies". In: *Clean-In-Place for Biopharmaceutical Processes*. Ed. by D. A. Seiberling. Volume 173. Informa Healthcare, 2008. Chap. 19, pp. 347–360. ISBN: 978-0-8493-4069-7.

[3] Z. M. Khoshhesab. "Reflectance IR Spectroscopy". In: *Infrared Spectroscopy - Materials Science, Engineering and Technology* (2012), pp. 233–244. DOI: 10.5772/37180.

[4] M. L. Hamilton, B. B. Perston, P. W. Harland, B. E. Williamson, M. a. Thomson, and P. J. Melling. "Grazing-angle fiber-optic IRRAS for in situ cleaning validation". In: *Organic Process Research and Development* 9.3 (2005), pp. 337–343. ISSN: 10836160. DOI: 10.1021/op040213z.

[5] M. Hamilton. "Applications of grazing-angle reflection absorption Fourier transform infrared spectroscopy to the analysis of surface contamination". In: January (2007), p. 233.

[6] *Application Note – AP0010612*. 2013.

[7] K. A. Baakev. *Process Analytical Technology*. Ed. by K. A. Bakeev. Second Edi. Oxford, UK: John Wiley & Sons Ltd., Aug. 2010. ISBN: 9780470988459. DOI: 10.1002/9780470988459.

[8]   I. Bisutti, I. Hilke, and M. Raessler. "Determination of total organic carbon – an overview of current methods". In: *TrAC Trends in Analytical Chemistry* 23.10-11 (Nov. 2004), pp. 716–726. ISSN: 01659936. DOI: `10.1016/j.trac.2004.09.003`.

[9]   L. S. Clescerl, A. E. Greenberg, and A. D. Eaton. *Standard Methods for the Examination of Water and Wastewater.* Ed. by L. S. Clescerl, A. E. Greenberg, and A. D. Eaton. 20th. American Public Health Association, American Water Works Association, Water Environment Federation, 1999. ISBN: 978-0875532356.

[10] P. Farrell, E. Blair, and T. Anderson. *Application of a Reagentless Direct Conductivity Online TOC Analyzer for Clean-in-Place Verification.* Tech. rep. Hach Company and McFlusion, Inc., 2009, pp. 1–6.

[11] International Organization for Standardization. *Optics and photonics - Spectral bands.* 2007.

[12] P. J. Larkin. *IR and Raman Spectroscopy - Principles and Spectral Interpretation.* Elsevier, 2011. ISBN: 9780123869845.

[13] G. Socrates. *Infrared and Raman Characteristic Group Frequencies.* Third. John Wiley & Sons Ltd., 2001. ISBN: 0471852988.

[14] B. C. Smith. *Fundamentals of Fourier Transform Infrared Spectroscopy.* Second. CRC Press, 2011. ISBN: 9781420069303.

[15] B. C. Smith. *Quantitative Spectroscopy: Theory and Practice.* Academic Press, 2002. ISBN: 0126503583.

[16] N. Sheppard. "The Historical Development of Experimental Techniques in Vibrational Spectroscopy". In: *Handbook of Vibrational Spectroscopy.* 2006. DOI: `10.1002/0470027320.s0101`.

[17] P. Griffiths and J. A. de Haseth. *Fourier Transform Infrared Spectrometry Second Edition.* Second. John Wiley & Sons Ltd., 2007. ISBN: 978-0-471-19404-0.

[18] H. Buijs. "Incandescent Sources for Mid- and Far-infrared Spectrometry". In: *Handbook of Vibrational Spectroscopy.* Ed. by J. M. Chalmers and P. R. Griffiths. John Wiley & Sons Ltd., 2002. ISBN: 9780471988472.

[19] G. P. Williams. "Infrared synchrotron radiation, review of properties and prospectives". In: *Proc. SPIE 3775, Accelerator-based Sources of Infrared and Spectroscopic Applications* 3775.July (1999), pp. 2–6. DOI: 10.1117/12.366630.

[20] G. P. Williams. "Synchrotron and Free Electron Laser Sources of Infrared Radiation". In: *Handbook of Vibrational Spectroscopy.* 2001. Chap. Synchrotro, pp. 371–378.

[21] B. G. Streetman and S. K. Banerjee. "Appendix III - Properties of Semiconductor Materials". In: *Solid State Electronic Devices.* Sixth Edit. Prentice-Hall, Inc., 2006. Chap. Appendix I, p. 540. ISBN: 978-81-203-3020-7.

[22] M. Tacke. "Lead-salt lasers". In: *Philosophical Transactions of the Royal Society A: Mathematical, Physical and Engineering Sciences* 359.1780 (2001), pp. 547–566. ISSN: 1364-503X. DOI: 10.1098/rsta.2000.0742.

[23] Y. Shani, A. Katzir, M. Tacke, and H. M. Preier. "Pb1-xSnxSe/Pb1-x-yEuySnxSe Corrugated Diode Laser". In: *IEEE Journal of Quantum Electronics* 25.8 (1989), pp. 1828–1844. DOI: 10.1109/3.34042.

[24] J. Faist, F. Capasso, D. L. Sivco, C. Sirtori, A. L. Hutchinson, and A. Y. Cho. "Quantum Cascade Laser". In: *Science* 264 (1994), pp. 553–556.

[25] G. Scamarcio, F. Capasso, C. Sirtori, J. Faist, A. L. Hutchinson, D. L. Sivco, and A. Y. Cho. "High-Power Infrared (8-Micrometer Wavelength) Superlattice Lasers". In: *Science* 276.5313 (May 1997), pp. 773–776. ISSN: 00368075. DOI: 10.1126/science.276.5313.773.

[26] J. Faist, M. Beck, T. Aellen, and E. Gini. "Quantum-cascade lasers based on a bound-to-continuum transition". In: *Applied Physics Letters* 78.2 (2001), p. 147. ISSN: 00036951. DOI: 10.1063/1.1339843.

[27] Z. Liu, D. Wasserman, S. S. Howard, A. J. Hoffman, C. F. Gmachl, X. Wang, T. Tanbun-ek, L. Cheng, and F.-s. Choa. "Room-Temperature Continuous-Wave Quantum Cascade Lasers Grown by MOCVD Without Lateral Regrowth". In: *IEEE Photonics Technology Letters* 18.12 (2006), pp. 1347–1349. DOI: 10.1109/LPT.2006.877006.

[28] C. F. Gmachl, F. Capasso, A. Tredicucci, D. L. Sivco, R. Köhler, A. L. Hutchinson, and A. Y. Cho. "Dependence of the Device Performance on the Number of Stages in Quantum-Cascade Lasers". In: *IEEE Journal of Selected Topics in Quantum Electronics* 5.3 (1999), pp. 808–816.

[29] K. J. Franz. *ErwinJr*. 2012.

[30] S. Birner. *nextnano3*. 2013.

[31] Muhammad A. Talukder, C. R. Menyuk, and F.-S. Choa. *QCL Simulation Package*. 2009.

[32] A. Y. Cho. "Morphology of Epitaxial Growth of GaAs by a Molecular Beam Method: The Observation of Surface Structures". In: *Journal of Applied Physics* 41.7 (1970), p. 2780. ISSN: 00218979. DOI: 10.1063/1.1659315.

[33] J. R. Arthur. "Molecular beam epitaxy". In: *Surface Science* 500.1-3 (Mar. 2002), pp. 189–217. ISSN: 00396028. DOI: 10.1016/S0039-6028(01)01525-4.

[34] K. Kosiel. "MBE - Technology for nanoelectronics". In: *Vacuum* 82.10 (June 2008), pp. 951–955. ISSN: 0042207X. DOI: 10.1016/j.vacuum.2008.01.033.

[35] S. Slivken, C. Jelen, A. Rybaltowski, J. Diaz, and M. Razeghi. "Gas-source molecular beam epitaxy growth of an 8.5 μm quantum cascade laser". In: *Applied Physics Letters* 71.18 (1997), p. 2593. ISSN: 00036951. DOI: 10.1063/1.119338.

[36] A. G. Thompson. "MOCVD technology for semiconductors". In: *Materials Letters* 30.4 (Mar. 1997), pp. 255–263. ISSN: 0167577X. DOI: 10.1016/S0167-577X(96)00215-7.

[37]   J. S. Roberts, R. P. Green, L. R. Wilson, E. a. Zibik, D. G. Revin, J. W. Cockburn, and R. J. Airey. "Quantum cascade lasers grown by metalorganic vapor phase epitaxy". In: *Applied Physics Letters* 82.24 (2003), p. 4221. ISSN: 00036951. DOI: 10.1063/1.1583858.

[38]   D. V. Shenai-Khatkhate, R. J. Goyette, R. L. DiCarlo Jr., and G. Dripps. "Environment, health and safety issues for sources used in MOVPE growth of compound semiconductors". In: *Journal of Crystal Growth* 272.1-4 (Dec. 2004), pp. 816–821. ISSN: 00220248. DOI: 10.1016/j.jcrysgro.2004.09.007.

[39]   G. P. Luo, C. Peng, H. Q. Le, S. S. Pei, W.-Y. Hwang, B. Ishaug, J. Um, J. N. Baillargeon, and C.-H. Lin. "Grating-tuned external-cavity quantum-cascade semiconductor lasers". In: *Applied Physics Letters* 78.19 (2001), p. 2834. ISSN: 00036951. DOI: 10.1063/1.1371524.

[40]   C. Peng, G. Luo, and H. Q. Le. "Broadband, continuous, and fine-tune properties of external-cavity thermoelectric-stabilized mid-infrared quantum-cascade lasers". In: *Applied Optics* 42.24 (2003), pp. 4877–4882. DOI: 10.1364/AO.42.004877.

[41]   H. Q. Le, G. W. Turner, J. R. Ochoa, M. J. Manfra, C. C. Cook, and Y.-H. Zhang. "Broad wavelength tunability of grating-coupled external cavity midinfrared semiconductor lasers". In: *Applied Physics Letters* 69.19 (1996), pp. 2804–2806. ISSN: 00036951. DOI: 10.1063/1.116849.

[42]   R. Maulini. "Broadly tunable mid-infrared quantum cascade lasers for spectroscopic applications par". PhD thesis. 2006.

[43]   T. M. Hard. "Laser wavelength selection and output coupling by a grating." In: *Applied Optics* 9.8 (Aug. 1970), pp. 1825–30. ISSN: 0003-6935.

[44]   A. Hugi, R. Terazzi, Y. Bonetti, A. Wittmann, M. Fischer, M. Beck, J. Faist, and E. Gini. "External cavity quantum cascade laser tunable from 7.6 to 11.4 μm". In: *Applied Physics Letters* 95.6 (2009), p. 061103. ISSN: 00036951. DOI: 10.1063/1.3193539.

[45] M. G. Littman and H. J. Metcalf. "Spectrally narrow pulsed dye laser without beam expander." In: *Applied Optics* 17.14 (July 1978), pp. 2224–7. ISSN: 0003-6935.

[46] C. Ye. *Tunable External Cavity Diode Lasers.* Ed. by T. K. Wei. Singapore: World Scientific Publishing Co. Pte. Ltd., 2004. ISBN: 9812560882.

[47] J. Faist, C. F. Gmachl, F. Capasso, C. Sirtori, D. L. Sivco, J. N. Baillargeon, and A. Y. Cho. "Distributed feedback quantum cascade lasers". In: *Applied Physics Letters* 70.20 (1997), pp. 2670–2672. ISSN: 00036951. DOI: 10.1063/1.119208.

[48] E. Mujagić, S. Schartner, L. K. Hoffmann, W. Schrenk, M. P. Semtsiv, M. Wienold, W. T. Masselink, and G. Strasser. "Grating-coupled surface emitting quantum cascade ring lasers". In: *Applied Physics Letters* 93.1 (2008), p. 011108. ISSN: 00036951. DOI: 10.1063/1.2958910.

[49] L. K. Hoffmann, M. Klinkmüller, E. Mujagić, M. P. Semtsiv, W. Schrenk, W. T. Masselink, and G. Strasser. "Tree array quantum cascade laser." In: *Optics express* 17.2 (2009), pp. 649–657. ISSN: 1094-4087. DOI: 10.1364/OE.17.000649.

[50] S. Ahn, C. Schwarzer, T. Zederbauer, D. C. MacFarland, H. Detz, A. M. Andrews, W. Schrenk, and G. Strasser. "High-power, low-lateral divergence broad area quantum cascade lasers with a tilted front facet". In: *Applied Physics Letters* 104.051101 (2014). ISSN: 0003-6951. DOI: 10.1063/1.4863504.

[51] E. Mujagić, L. K. Hoffmann, S. Schartner, M. Nobile, W. Schrenk, M. P. Semtsiv, M. Wienold, W. T. Masselink, and G. Strasser. "Low divergence single-mode surface emitting quantum cascade ring lasers". In: *Applied Physics Letters* 93.16 (2008), p. 161101. ISSN: 00036951. DOI: 10.1063/1.3000630.

[52] M. Brandstetter, A. Genner, K. Anic, and B. Lendl. "Tunable Mid-IR lasers: A new avenue to robust and versatile physical chemosensors". In: *Procedia Engineering* 5 (2010), pp. 1001–1004. ISSN: 18777058. DOI: 10.1016/j.proeng.2010.09.278.

[53] A. Genner. "Charakterisierung eines External Cavity-Quantenkaskadenlasers und Aufnahme von Spektren". Bachelor Thesis. Vienna University of Technology, 2010.

[54] "Daylight Solutions Inc." *Tunable Mid-IR External Cavity Laser System.* 2009.

[55] C. Wagner, A. Genner, G. Ramer, and B. Lendl. "Advanced Total Lab Automation System (ATLAS)". In: *Modeling, Programming and Simulations Using LabVIEW^{TM} Software.* Ed. by R. De Asmundis. InTech, 2011. Chap. 1, pp. 3–20. ISBN: 978-953-307-521-1. DOI: 10.5772/564.

[56] "Daylight Solutions Inc." *EC-QCL Specifications 11088-015-A0118.* 2009.

[57] W. Tomischko and B. Lendl. "Ein vereinfachtes Boxcar-Integrator-System für Prozessanwendungen mit Gatesteuerung unter Verwendung von Standardbauelementen". In: *Informationstagung Mikroelektronik 12.* 2012, pp. 71–74. ISBN: 978-3-85133-071-7.

[58] A. Genner, M. Brandstetter, W. Tomischko, and B. Lendl. *Signal processing strategies for liquid phase sensors based on external cavity quantum cascade lasers.* 2010.

[59] National Instruments. *Application Design Patterns: State Machines.* Tech. rep. National Instruments, 2011.

[60] National Instruments. *Application Design Patterns: Producer/Consumer.* Tech. rep. National Instruments, 2012.

[61] R. Christoph, B. Schmidt, U. Steinberner, W. Dilla, and R. Karinen. "Glycerol". In: *Ullmann's Encyclopedia of Industrial Chemistry.* 17th ed. 2006, pp. 67–82. ISBN: 9783527306732. DOI: 10.1002/14356007.a12.

[62] A. C. J. Voragen, C. Rolin, B. U. Marr, I. Challen, A. Riad, R. Lebbar, and S. H. Knutsen. "Polysaccharides". In: *Ullmann's Encyclopedia of Industrial Chemistry.* 29th ed. 2003, pp. 417–474. ISBN: 9783527306732. DOI: 10.1002/14356007.a21.

[63] A. Barth. "Infrared spectroscopy of proteins." In: *Biochimica et biophysica acta* 1767.9 (Sept. 2007), pp. 1073–101. ISSN: 0006-3002. DOI: `10.1016/j.bbabio.2007.06.004`.

[64] B. Schwarz, P. Reininger, H. Detz, T. Zederbauer, A. Maxwell Andrews, S. Kalchmair, W. Schrenk, O. Baumgartner, H. Kosina, and G. Strasser. "A bifunctional quantum cascade device for same-frequency lasing and detection". In: *Applied Physics Letters* 101.19 (2012), pp. 191109.1–4. ISSN: 00036951. DOI: `10.1063/1.4767128`.

[65] B. Schwarz, P. Reininger, H. Detz, T. Zederbauer, A. M. Andrews, W. Schrenk, and G. Strasser. "Monolithically integrated mid-infrared quantum cascade laser and detector." In: *Sensors (Basel, Switzerland)* 13.2 (Jan. 2013), pp. 2196–205. ISSN: 1424-8220. DOI: `10.3390/s130202196`.

[66] C. Schwarzer, E. Mujagić, S. I. Ahn, A. M. Andrews, W. Schrenk, W. Charles, C. Gmachl, and G. Strasser. "Grating duty-cycle induced enhancement of substrate emission from ring cavity quantum cascade lasers". In: *Applied Physics Letters* 100.19 (2012), p. 191103. ISSN: 00036951. DOI: `10.1063/1.4712127`.

[67] Georg Thieme Verlag. *Römpp Online - Glycerol.*

[68] Georg Thieme Verlag. *Römpp Online - Xanthan.*

[69] S. Kromidas. *Handbuch Validierung in der Analytik.* WILEY-VCH Verlag, 2008. ISBN: 9783527298112.

[70] T. Siegmann-Hegerfeld, A. Genner, M. Brandstetter, B. Lendl, and M. Harasek. "Online Monitoring of TOC Contaminations in Clean- in-Place Processes for Optimized Process Control , Increased Process Efficiency and Quality". In: *Chemical Engineering Transactions* 35 (2013), pp. 979–984. DOI: `10.3303/CET1335163`.

[71]   G. Wysocki, R. Curl, F. Tittel, R. Maulini, J. Bulliard, and J. Faist. "Widely tunable mode-hop free external cavity quantum cascade laser for high resolution spectroscopic applications". In: *Applied Physics B* 81 (Sept. 2005), pp. 769–777. ISSN: 0946-2171. DOI: `10.1007/s00340-005-1965-4`.

[72]   T. Tsai and G. Wysocki. "External-cavity quantum cascade lasers with fast wavelength scanning". In: *Applied Physics B* 100 (Jan. 2010), pp. 243–251. ISSN: 0946-2171. DOI: `10.1007/s00340-009-3865-5`.

[73]   M. Brandstetter, C. Koch, A. Genner, and B. Lendl. "Measures for optimizing pulsed EC-QC laser spectroscopy of liquids and application to multi-analyte blood analysis". In: *Proc. SPIE* 8993 (2014). DOI: `10.1117/12.2038585`.

[74]   M. C. Phillips, M. S. Taubman, B. E. Bernacki, B. D. Cannon, R. D. Stahl, J. T. Schiffern, and T. L. Myers. "Real-time trace gas sensing of fluorocarbons using a swept-wavelength external cavity quantum cascade laser". In: *The Analyst* (Jan. 2013). ISSN: 1364-5528. DOI: `10.1039/c3an01642k`.

[75]   B. Lee, M. Belkin, C. Pflügl, L. Diehl, H. Zhang, R. Audet, J. MacArthur, D. Bour, S. Corzine, G. Hufler, and F. Capasso. "DFB Quantum Cascade Laser Arrays". In: *IEEE Journal of Quantum Electronics* 45.5 (May 2009), pp. 554–565. ISSN: 0018-9197. DOI: `10.1109/JQE.2009.2013175`.

[76]   E. Mujagić, C. Schwarzer, Y. Yao, J. Chen, C. Gmachl, and G. Strasser. "Two-dimensional broadband distributed-feedback quantum cascade laser arrays". In: *Applied Physics Letters* 98.14 (2011), p. 141101. ISSN: 00036951. DOI: `10.1063/1.3574555`.

[77]   P. Jouy, M. Mangold, B. Tuzson, L. Emmenegger, Y.-C. Chang, L. Hvozdara, H. P. Herzig, P. Wägli, A. Homsy, N. F. de Rooij, A. Wirthmueller, D. Hofstetter, H. Looser, and J. Faist. "Mid-infrared spectroscopy for gases and liquids based on quantum cascade technologies." In: *The Analyst* (Oct. 2013). ISSN: 1364-5528. DOI: `10.1039/c3an01462b`.

[78]   B. Schwarz, P. Reininger, D. Ristanić, H. Detz, A. M. Andrews, W. Schrenk, and G. Strasser. "Monolithically integrated mid-infrared lab-on-a-chip using plasmonics and quantum cascade structures." In: *Nature communications* 5.May (Jan. 2014), p. 4085. ISSN: 2041-1723. DOI: 10.1038/ncomms5085.

Publications

[1] M. Brandstetter, A. Genner, K. Anic, and B. Lendl. "Tunable Mid-IR lasers: A new avenue to robust and versatile physical chemosensors". In: *Procedia Engineering* 5 (2010), pp. 1001–1004. ISSN: 18777058. DOI: 10.1016/j.proeng.2010.09.278.

[2] M. Brandstetter, A. Genner, K. Anic, and B. Lendl. "Tunable external cavity quantum cascade laser for the simultaneous determination of glucose and lactate in aqueous phase". In: *The Analyst* 135.12 (Dec. 2010), pp. 3260–3265. ISSN: 1364-5528. DOI: 10.1039/c0an00532k.

[3] C. Wagner, A. Genner, G. Ramer, and B. Lendl. "Advanced Total Lab Automation System (ATLAS)". In: *Modeling, Programming and Simulations Using LabVIEW^{TM} Software.* Ed. by R. De Asmundis. InTech, 2011. Chap. 1, pp. 3–20. ISBN: 978-953-307-521-1. DOI: 10.5772/564.

[4] M. Brandstetter, A. Genner, L. Volgger, C. Jungbauer, and B. Lendl. "Direct determination of glucose, lactate and triglycerides in blood serum by a tunable quantum cascade laser-based mid-IR sensor". In: *Applied Physics B: Lasers and Optics* (2012). DOI: 10.1007/s00340-012-5080-z.

[5] M. Brandstetter, T. Sumalowitsch, A. Genner, A. E. Posch, C. Herwig, A. Drolz, V. Fuhrmann, T. Perkmann, and B. Lendl. "Reagent-free monitoring of multiple clinically relevant parameters in human blood plasma using a mid-infrared quantum cascade laser based sensor system." In: *The Analyst* 138.14 (June 2013), pp. 4022–8. ISSN: 1364-5528. DOI: 10.1039/c3an00300k.

[6] T. Siegmann-Hegerfeld, A. Genner, M. Brandstetter, B. Lendl, and M. Harasek. "Online Monitoring of TOC Contaminations in Clean- in-Place Processes for Optimized Process Control , Increased Process Efficiency and Quality". In: *Chemical Engineering Transactions* 35 (2013), pp. 979–984. DOI: 10.3303/CET1335163.

[7] M. R. EL-Zahry, A. Genner, I. H. Refaat, H. a. Mohamed, and B. Lendl. "Highly reproducible SERS detection in sequential injection analysis: Real time preparation and application of photo-reduced silver substrate in a moving flow-cell". In: *Talanta* 116 (Nov. 2013), pp. 972–977. ISSN: 00399140. DOI: 10.1016/j.talanta.2013.07.059.

[8] C. Schwarzer, R. Szedlak, L. Burgstaller, A. Genner, T. Zederbauer, H. Detz, A. M. Andrews, W. Schrenk, and G. Strasser. "Polarization Versatility of Surface Emitting Ring Cavity Quantum Cascade Lasers". In: *Lasers and Electro-Optics Europe (CLEO EUROPE/IQEC)* (2013). DOI: 10.1109/CLEOE-IQEC.2013.6800693.

[9] M. Brandstetter, T. Sumalowitsch, A. Genner, V. Fuhrmann, and B. Lendl. "Clinical Application of a Mid-Infrared Quantum Cascade Laser Based Sensor for Multianalyte Detection in Human Blood Plasma". In: *CLEO: Applications and Technology*. OSA, 2013. ISBN: 978-1-55752-972-5. DOI: 10.1364/CLEO{_}AT.2013.AF1L.3.

[10] M. Brandstetter, A. Genner, C. Schwarzer, E. Mujagić, G. Strasser, and B. Lendl. "Time-resolved spectral characterization of ring cavity surface emitting

and ridge-type distributed feedback quantum cascade lasers by step-scan FT-IR spectroscopy". In: *Optics Express* 22.3 (2014). DOI: 10.1364/OE.22.002656.

[11]   M. Brandstetter, C. Koch, A. Genner, and B. Lendl. "Measures for optimizing pulsed EC-QC laser spectroscopy of liquids and application to multi-analyte blood analysis". In: *Proc. SPIE* 8993 (2014). DOI: 10.1117/12.2038585.

[12]   H. Moser, A. Genner, J. Ofner, G. Strasser, and B. Lendl. "The application of a ring cavity surface emitting (RCSE) quantum cascade laser on the measurement of H2S in a CH4 matrix for process analytics". In: *Optics Express* 24.6 (2016), pp. 6572–6585. DOI: 10.1364/OE.24.006572.

Posters

[1] M. Brandstetter, A. Genner, and B. Lendl. *Nanosecond step-scan FTIR spectroscopy of a pulsed external-cavity quantum-cascade laser.* 2009.

[2] M. Brandstetter, A. Genner, K. Anic, and B. Lendl. *Quantum Cascade Lasers : A New Avenue to Robust and Versatile Sensors for Bodily Fluids.* 2010.

[3] A. Genner, M. Brandstetter, W. Tomischko, and B. Lendl. *Signal processing strategies for liquid phase sensors based on external cavity quantum cascade lasers.* 2010.

[4] M. Brandstetter, L. Volgger, E. Aguilera-herrador, A. Genner, and B. Lendl. *Demonstration of an external-cavity quantum cascade laser based blood sensor.* 2010.

[5] M. Brandstetter, A. Genner, L. Volgger, and B. Lendl. *Liquid phase analysis using a pulsed external cavity quantum cascade laser for mid-IR spectroscopy.* 2011.

[6] M. Brandstetter, G. Ramer, A. Genner, J. Kasberger, and B. Lendl. *Robust mid-IR spectroscopy using a pulsed external cavity QCL for liquid phase analysis.* 2011.

[7] W. Tomischko, C. Reidl-Leuthner, A. Genner, and B. Lendl. *A Low Budget High Precision Driver for Pulsed Quantum Cascade Lasers.* 2012.

[8] M. Brandstetter, V. Fuhrmann, A. Genner, and B. Lendl. *Blood Monitoring with an External Cavity Quantum Cascade Laser.* 2012.

[9] A. Genner, M. Brandstetter, M. Harasek, and B. Lendl. *Monitoring Industrial Processes Using a Sensor Based on an External Cavity-Quantum Cascade Laser.* 2012.

[10] H. Moser, M. Brandstetter, A. Genner, E. Mujagić, G. Strasser, and B. Lendl. *Time-resolved characterization of the spectral behavior of ring cavity surface emitting QCLs (RCSE-QCLs).* 2012.

[11] M. Brandstetter, T. Sumalowitsch, A. Genner, V. Fuhrmann, Thomas Perkmann, and B. Lendl. *Tunable Quantum Cascade Laser based Blood Sensor for Clinical Application.* 2012.

[12] A. Genner, M. Brandstetter, M. Harasek, and B. Lendl. *Online Monitoring of Cleaning In Place Systems Facilitated by a Broadly Tuneable Quantum Cascade Laser.* 2012.

[13] H. Moser, A. Genner, J. Ofner, and B. Lendl. *Hydrogen Sulfide (H2S) Sensing using Ring Cavity Surface Emitting QCLs (RCSE-QCLs) around 8um.* 2014.

[14] A. Genner, C. Gasser, H. Moser, T. Sumalowitsch, J. Ofner, and B. Lendl. *Online Monitoring of an Industrial Process: Application of a Fabry-Pérot Detector Based Sensor.* 2014.

[15] C. Gasser, A. Genner, H. Moser, J. Ofner, and B. Lendl. *Tunable Fabry-Perot Detectors for Process Analytical Chemistry - Evaluation of a Prototype for Multi-Component Gas Streams.* 2015.